

7. Synthesis of PbS and SnO_x nanoparticles for functional applications

The synthesis of semiconducting material (PbS) via the evaporation-condensation route is undertaken in combination with the control techniques described in the preceding chapter such as size fractionation and on-line particle size measurements. By means of an on-line measurement of the agglomerate diameter the evaporation and sintering characteristics of PbS nanoparticles are investigated and reported in Chapter 7.1. The measurements allow to obtain a theoretical description of the evaporation and sintering process. Strictly speaking, the particles are sublimating but generally the term evaporation is used. These experiments have partly been published in Kruis *et al.* (1998c) and the evaluation of the sintering appeared in Kruis *et al.* (2000b). Similar synthesis experiments for obtaining SnO_x nanoparticles for gas-sensing applications will be reported in Chapter 7.2.

Quantum confinement effects in semiconducting nanocrystals have been widely studied since Brus in 1983 focussed the attention of the scientific community on this phenomenon (Brus, 1983). Almost all investigations have been done for colloid systems, i.e. in the liquid phase. For most practical applications, these particles will, however, have to be supported on a substrate. The gas-phase techniques described in this Habilitation Thesis are ideally suited for this, as both synthesis and deposition are done in the gas phase. For the system chosen in this work, PbS, the confinement effects have until now only been reported for PbS nanoparticles synthesized in the liquid phase. In Chapter 7.3 optical absorption spectra indicative for quantum confinement effects in size-fractionated PbS nanoparticles from the gas phase will be shown.

Finally, an experimental method to obtain well-defined composite aggregates of size-selected nanoparticles in the gas phase is proposed. Such composite aggregates are interesting for applications in which the properties of semiconducting nanoparticles are modified by addition of another nanoparticle material. A well-known example is the addition of Pt nanoparticles to SnO₂ nanostructured material, which increases the sensitivity of the gas sensor, presumably due to catalytic surface reactions on the Pt. As a model for the composite system semiconductor-metal, PbS-Ag is chosen here, as for both materials exists experience with the synthesis. Both materials are synthesized separately by nucleation and aggregation processes in a furnace reactor. The two oppositely charged aerosols which have been size-selected on the basis of their

electrical mobility are mixed. The fact that nanoaggregates which contain the two different materials are uncharged is used in order to separate them from unaggregated particles and aggregates containing only one component. A paper dedicated to this subject has been published (Maisels *et al.*, 2000).

7.1 Preparation of size-classified PbS nanoparticles in the gas phase

Nanocrystals of semiconducting materials can exhibit quantum-size effects when the particle size becomes comparable to or smaller than the spatial extent of the wavefunctions of electrons or holes. This results in a blue shift in the optical absorption spectrum (Brus, 1984). A size uniformity is important in order to study or make use of quantum size effects, as a distribution of particle sizes will decrease these effects.

The synthesis of nanocrystals in the vapor phase has several advantages over other methods such as controlled chemical purity and the generation of clusters with free surfaces (Saunders *et al.*, 1992). Size-selection has been proven to be also possible in the gas phase and was applied to produce Si (Camata *et al.*, 1996) and GaAs (Deppert *et al.*, 1996) nanocrystals. However, the lower atomic mobilities in the solid phase can inhibit crystallization of the particles and the stoichiometry of the material is in some systems difficult to maintain (Saunders *et al.*, 1992).

The generation of nearly monodisperse PbS nanocrystals in the gas phase is demonstrated in this subchapter. PbS is a narrow-gap IV-VI semiconductor with a cubic rock salt structure. PbS is an attractive candidate for the study of quantum confinement effects as its hole Bohr radius is 9 nm. This results in strong confinement effects as compared to the II-VI semiconductors such as CdS and CdSe with Bohr radii of about 1 nm (Machol *et al.*, 1994).

Previously reported syntheses of PbS nanocrystals with sizes below 20 nm are all performed in a liquid phase. They include controlled precipitation in polyvinylalcohol (Nenadovic *et al.*, 1990), sol-gel synthesis (Gacoin *et al.*, 1995), synthesis on Langmuir monolayers (Zhao and McCormick, 1992) and electrostatically spraying a PbNO₃ solution in a H₂S atmosphere (Salata *et al.*, 1994a). Earlier studies on gas-phase synthesis reported loss of stoichiometry due to dissociation when directly evaporating PbS in Ar (Kaito *et al.*, 1987). On the other hand, it is known that the IV-VI semiconductors evaporate essentially in a molecular form (El-Rahaiby and Rao, 1982), and that film formation of stoichiometric IV-VI compounds is possible by direct evaporation (Lopez-Otero,

1987). Hereby, the tendency to dissociate is smaller the lower the evaporation temperature and the higher the pressure.

7.1.1 Experiments

In the present work a gas-phase synthesis method is used at normal pressure for the preparation of sub-20 nm, crystalline, quasi-spherical, monodisperse PbS particles. Heating a furnace containing the PbS powder at temperatures between 600°C and 700°C resulted in appreciable particle formation as measured with a condensation nucleus counter. These particles are formed by homogeneous nucleation and subsequent aggregation by Brownian motion. Transmission electron micrographs showed amorphous and partially sintered particles with a standard deviation between 1.4 and 1.6, typical for gas-phase synthesis.

In order to obtain crystalline and spherical particles, the aerosol flow was passed initially through a second furnace. Electron micrographs showed crystalline particles, which were however mostly present in aggregates consisting of several quasi-spherical particles bonded together by amorphous material. Therefore, it can be concluded that the particle number concentration is too high when the aerosol enters the second furnace, causing aggregation at the same time crystallization and sintering are taking place.

The experimental setup was then changed to that depicted in Fig. 7.1.1. It contains six elements: a nanocrystal source, an aerosol charger, a size classifier, a tube furnace, an electrostatic precipitator and a particle size measurement system consisting of a Differential Mobility Analyzer (DMA) and a condensation nucleus counter. Fig. 7.1.1 shows a schematic diagram of the setup, which is similar to that used by Deppert *et al.* (1994). A PbS aerosol is formed by sublimating a PbS powder in a tube furnace and after dilution (1:2) charged by a radioactive β -source (Kr⁸⁵). Nitrogen obtained from evaporating liquid nitrogen is used as carrier gas. The total gas flow was kept at 1.5 l/min by means of mass flow controllers (MFC), and the system is operated at atmospheric pressure. In a Differential Mobility Analyzer the charged particles are size-selected on the basis of their electric mobility, which is a function of their charge level, mass and shape. The mobility equivalent diameter based hereon is defined as the diameter D_m related to the Stokes-Cunningham formula (Hinds, 1982) and is equal to the geometric diameter when the particles are singly charged and spherical. The DMA (NANO-DMA, TSI, Minneapolis, USA) is capable of delivering monodisperse aerosols with sizes adjustable between 2 and 50 nm and standard deviations between 1.05 and 1.20, depending on the flow conditions in the apparatus (Chen *et al.*, 1998).

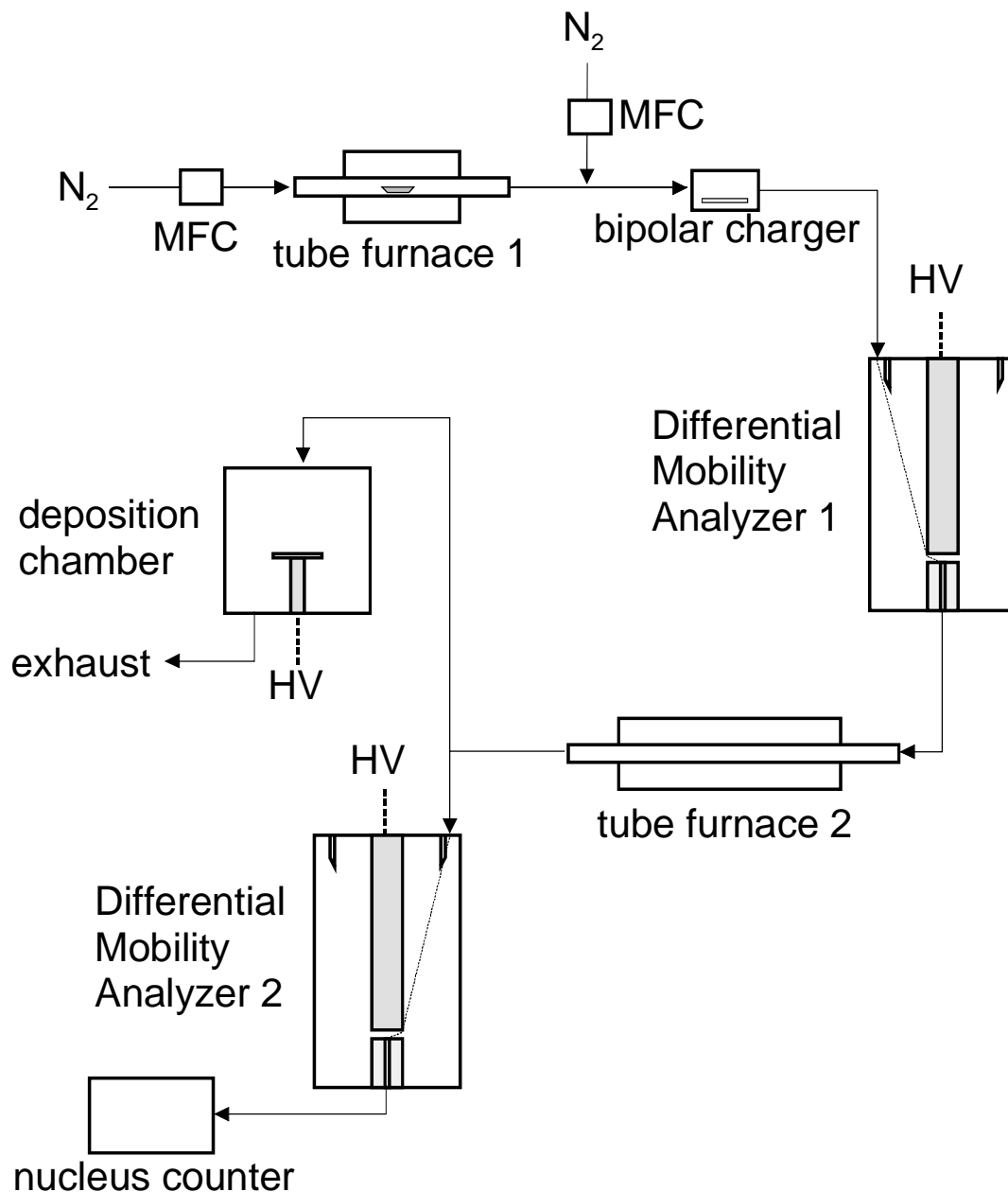


Fig. 7.1.1. Schematic drawing of the experimental setup for gas-phase synthesis and size fractionation of PbS nanocrystals. Particles are generated in tube furnace 1, charged by means of a bipolar charger, size-fractionated utilizing a first Differential Mobility Analyzer (DMA), sintered in tube furnace 2 and deposited onto a substrate within a deposition chamber. A second DMA, in combination with a nucleus counter, is used to measure the particle size distribution. The N₂ gas flow is controlled by mass flow controllers (MFCs).

In our studies, the flow ratio was chosen to get a theoretical distribution in diameter of $\pm 0.1 D_m$.

An electrostatic precipitator enables the aerosol to be deposited with nearly 100 % efficiency on a substrate placed in a high-voltage field. A condensation nucleus counter (3025, TSI, Minneapolis, USA) with a lower detection limit of 3 nm enables the monitoring of the aerosol number concentration. By means of a second DMA after the second furnace it is possible to detect on-line the change in mobility diameter due to the passage through the second furnace.

As the sintering step now takes place after the size fractionation, the particle number concentration in the second furnace is roughly two decades smaller, thus decreasing the rate of aggregation during the crystallization and sintering step. The smaller number concentration has two causes: the charging efficiency in the radioactive charger, which is only 5 % for particle with diameter of 10 nm, and the size fractionation, which takes out part of the size spectrum. The final production rates of sintered particles with initial mobility diameters $D_m^{unsintered} = 15$ nm (sintered at 400°C) and $D_m^{unsintered} = 50$ nm (sintered at 500°C) are $3 \cdot 10^4/\text{cm}^3$ and $10^5/\text{cm}^3$, respectively. Typical electron micrographs now showed single crystalline particles.

The second furnace proved to be necessary to obtain monocrystalline particles. Above 350°C, crystalline particles were detected by XRD, with the crystallite size increasing with sintering temperature. In Fig.7.1.2 a HRTEM micrograph of a monocrystalline PbS nanoparticle is shown, as obtained after sintering a particle fraction with an initial mobility diameter of 50 nm.

However, at too high temperatures the particles evaporated. This can be seen in Fig. 7.1.3, which shows a size distribution for particles having initially a mobility diameter of 15 nm. Strictly speaking, the word size distribution is not correct as the curves are not corrected for the transfer function of the DMA and the charging efficiency. For our purposes, however, the exact form of the size distribution before the charger and DMA is not of interest, what is important is the yield of particles after the size fractionation, as the DMA is an integral part of our synthesis setup. The amorphous nature of the particles makes sintering however necessary. It can be seen that the mean mobility diameter shifts to smaller sizes. This is due to the compaction process caused by restructuring, sintering and crystallization. Restructuring and sintering processes are known to lead to a smaller mobility equivalent diameter with increasing temperature (Schmidt-Ott, 1988). This is due to increased solid state diffusion coefficients which result in more compact particles. The total number concentration of particles decreases at increasing sintering temperatures because of increased thermophoretic losses when exiting the furnace, and at the highest temperature also because of evaporation.

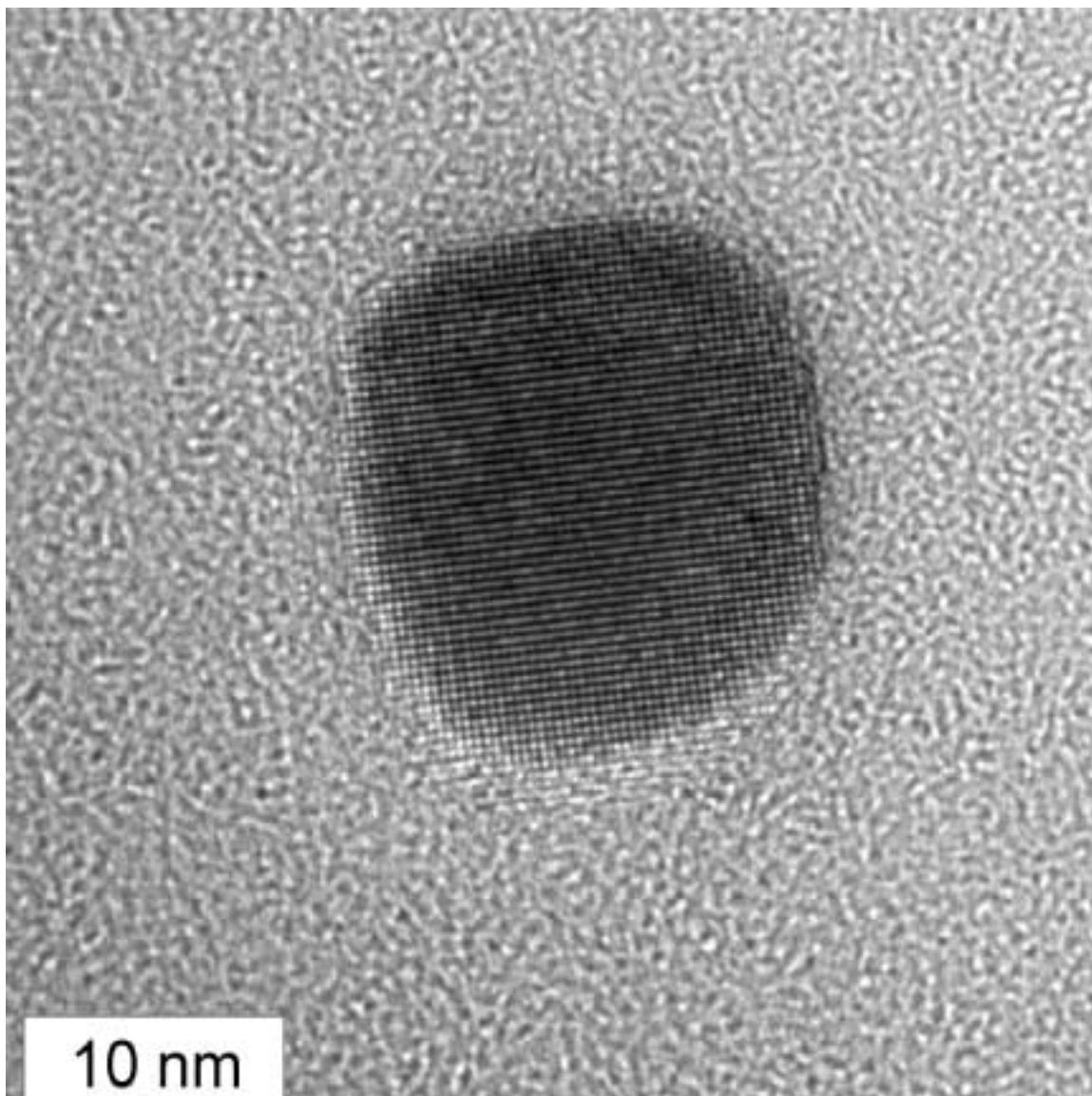


Fig.7.1.2. HRTEM micrograph of a monocrystalline PbS nanoparticle.

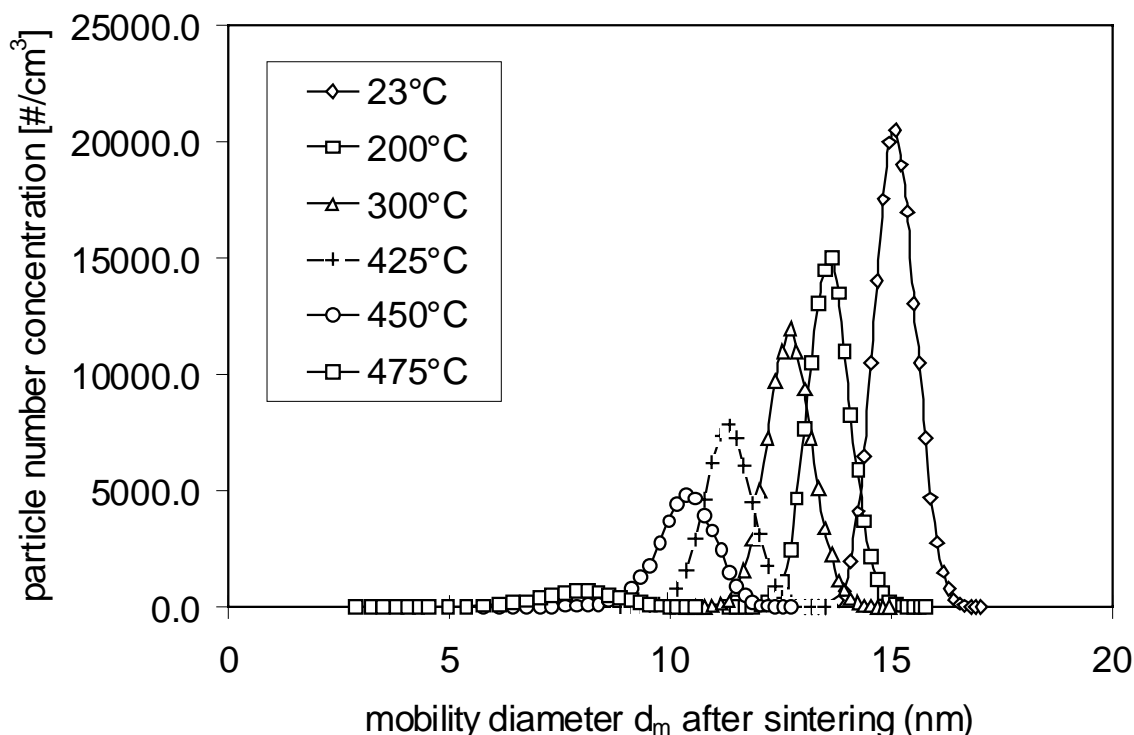


Fig. 7.1.3. Size distribution of size-selected PbS nanoparticles ($d_m = 15$ nm) as a function of sintering temperature.

The mean mobility diameter as a function of sinter temperature is shown in Fig. 7.1.4 for PbS particles having different initial mobility diameters. It can be seen that initially larger particles show a higher decrease in mobility diameter, indicating an increased compaction rate. This is confirmed by TEM microscopy, from which we observe a more porous and open structure containing tens of primary particles for the larger unsintered aggregates, which can be stronger compacted due to sintering. Smaller particles contain however few primary particles and are therefore more compact, which means that they can be less easily compacted. At the highest temperature used, the particle size decreases rapidly.

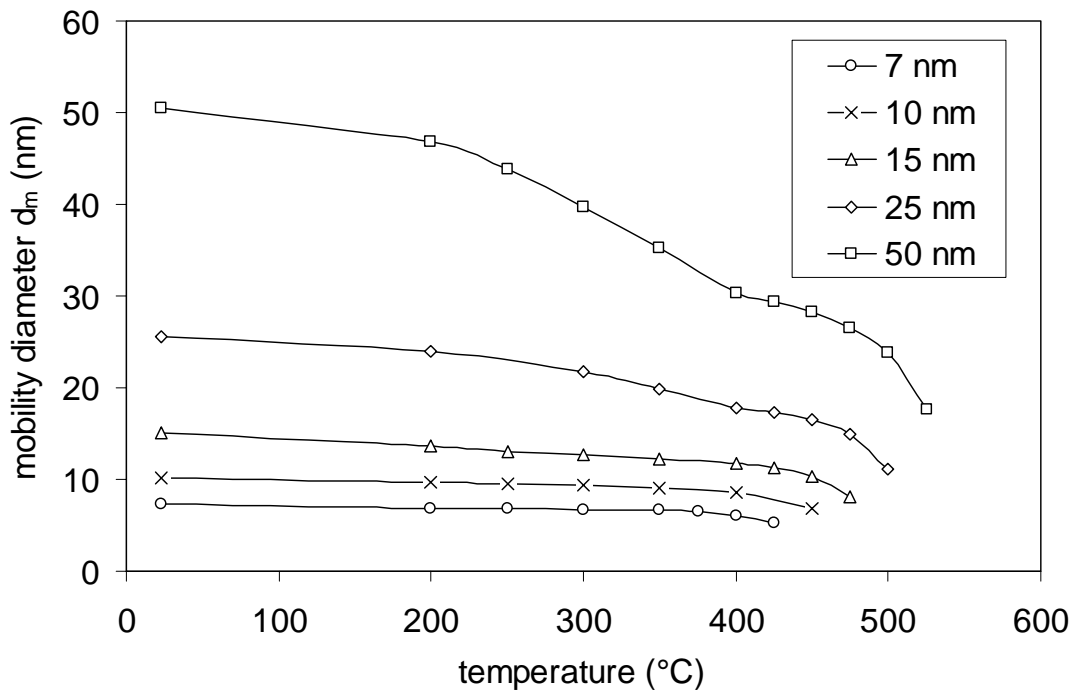


Fig. 7.1.4. Mobility diameter of PbS nanoparticles with different initial mobility diameters as function of the sintering temperature.

This is accompanied by a rapid increase in the half-width of the size distribution, Fig. 7.1.5. The width of the size distribution increases above a certain threshold temperature which is a function of the initially selected mobility diameter. We attribute this to evaporation, which destroys the original size distribution and can also lead to new particle formation. The origin of the local maximum in the curves for mobility diameters of 25 and 50 nm is not quite clear, but might be due to coagulation in the sinter furnace as large porous particles have an increased coagulation probability at higher temperatures.

The necessity of sintering to obtain spherical particles is clearly seen in Fig. 7.1.6, where electron micrographs of particles with $D_m^{unsintered} = 50$ nm, sintered at 300°C (A) and at 500°C (B), are shown. The larger ‘volume’ of the agglomerates in Fig. 7.1.6A as compared to the spherical particles in Fig. 7.1.6B supports our suggestion that evaporation takes place. From the electron micrographs of quasi-spherical sintered particles (comparable to those in Fig. 7.1.6B), we have determined size distributions of the particles (Fig. 7.1.7). Although the agglomerates shown in Fig. 7.1.6A exhibit a very irregular morphology, we obtain a rather narrow size distribution with a standard deviation of 1.13 for the quasi-

spherical particles. The smallest particles obtained with the procedure described above have a diameter of some 3 nm.

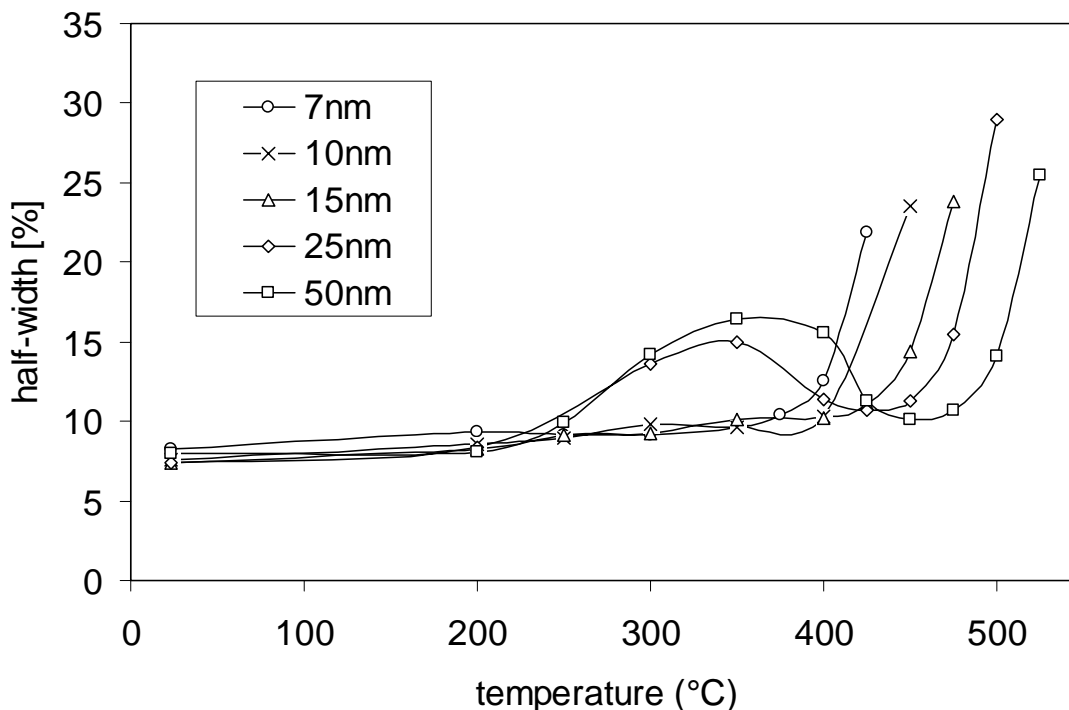


Fig. 7.1.5. Half-width of the size-fractionated distribution after sintering.

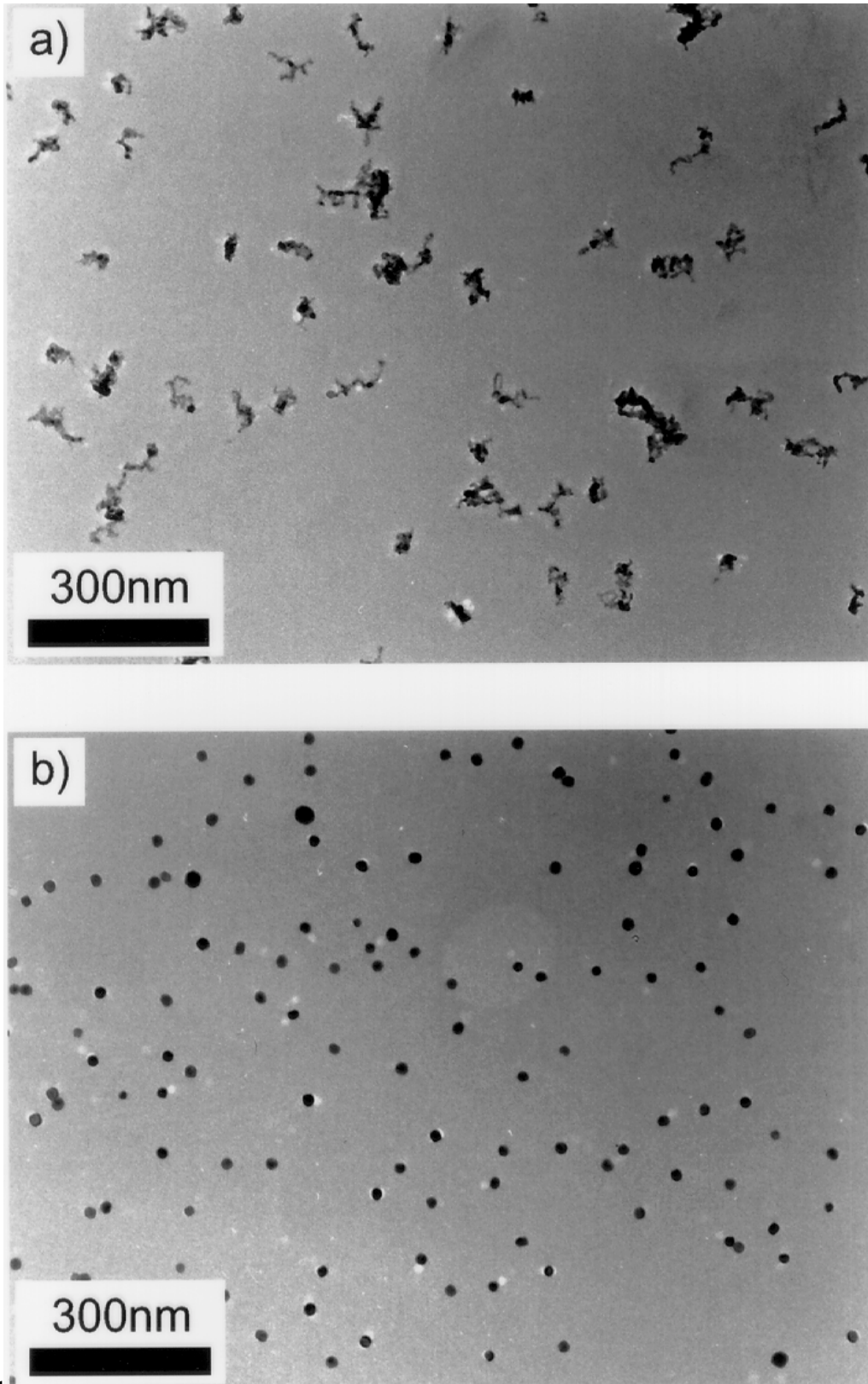
Electron diffraction and X-ray diffraction (XRD) were used to confirm the crystallinity of the PbS samples. A lattice constant of $5.945 \pm 0.005 \text{ \AA}$ was determined using X-ray diffraction, being within 0.15 % of the bulk value for PbS (Pearson, 1967). No Pb nor Pb-S-O compounds were detected. Line broadening of the diffraction pattern was used to determine the grain size. Since the grain size as determined from XRD is in good agreement with the particle size as taken from the TEM investigations, the PbS nanoparticles are to be considered monocrystalline. This is furthermore supported by the observation that the particles show faceting.

From the experimental results, it becomes clear that the sublimation and sintering temperatures have to meet the following conditions:

$$T_{\text{high nucleation rate}} < T_{\text{furnace for sublimation}} < T_{\text{stoichiometric evaporation}}$$

and

$$T_{\text{appreciable sintering}} < T_{\text{furnace for sintering}} < T_{\text{appreciable evaporation}}$$



and

Fig. 7.1.6. Electron micrographs of PbS particles with $D_m^{\text{unsintered}} = 50 \text{ nm}$ sintered at (a) 300°C and (b) 500°C .

Fulfilling the first condition ensures that a sufficient number of particles is formed by homogeneous nucleation at temperatures lower than the temperature where off-stoichiometric evaporation starts. For InP and GaAs e.g., this relation is not fulfilled (Deppert *et al.*, 1998). The second relation is clear from the earlier description of the experiments: crystalline and quasi-spherical particles have to be obtained by sintering at temperatures which do not cause extensive evaporation. For PbS, there is for each particle size a temperature range of some 50 K where the sintering rate is appreciable while at the same time the evaporation rate is such that the particles shrink but do not disappear. The optimum sintering temperature turns out to be 400°C for particles having a mobility equivalent diameter of 15 nm and 500°C for particles having a mobility equivalent diameter of 50 nm.

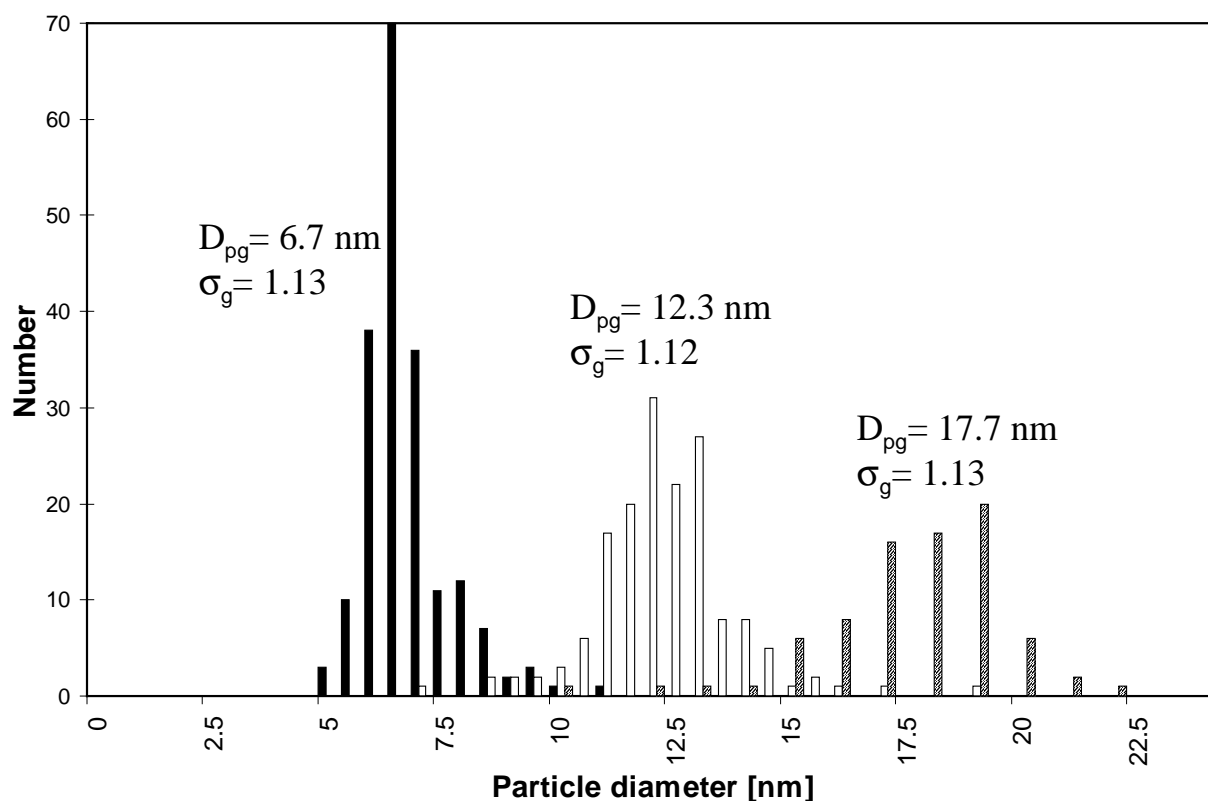


Fig. 7.1.7. Size distributions determined from electron micrographs for particles synthesized under optimized conditions ($D_m^{unsintered} = 15$ nm sintered at 400°C, $D_m^{unsintered} = 25$ nm sintered at 475°C and $D_m^{unsintered} = 50$ nm sintered at 500°C). Residual agglomerates (~5% of all particles) were not taken into account.

7.1.2 Analysis of evaporation and sintering mechanisms of PbS

In order to assess the evaporation mechanism, the evaporation rate of a PbS particle is calculated using the following formula (Hinds, 1982):

$$\frac{dd_p}{dt} = \frac{4D_v M}{R\rho_p d_p} \left(\frac{p_\infty}{T_\infty} - \frac{p_s}{T_s} \right) \frac{2\lambda + d_p}{d_p + 5.33 \frac{\lambda^2}{d_p} + 3.42 \lambda} \quad (7.1.1)$$

where D_v is the diffusion coefficient of the vapor, M is the molecular weight of the particle, R is the gas constant, ρ_p is the particle density, d_p is the particle size, p_∞ and p_s refer to the partial pressure in the background gas and at the particle surface, T is the temperature and λ is the mean free path of the gas. p_∞ is assumed to be negligible in comparison to p_s , for which we use the vapor pressure of PbS, fitted from data in the range 755–1108°C (Gmelin, 1979):

$$\log p(\text{Torr}) = -1.126 \cdot 10^5 \frac{1}{T(\text{K})} + 5.80910^{-4} T(\text{K}) + 9.3531 \quad (7.1.2)$$

The resulting evaporation rates are shown in table 7.1.1. As can be seen from the table, the evaporation rate is only a slight function of the particle size. With a residence time of 6 s in the second furnace, the calculations on the evaporation rate of the PbS nanoparticles predict a decrease in particle diameter of 2.2 nm (@450°C), 7.2 nm (@475°C), 23 nm (@500°C) and 65 nm (@525°C). This corresponds well with the experimental observation, e.g. particles with an initial mobility diameter of 15 nm have completely disappeared with a furnace temperature of 500°C.

Table 7.1.1. Evaporation rates $\frac{dd_p}{dt}$ (nm/s) of PbS nanoparticles.

Evaporation rate (nm/s)	Temperature (°C)				
	425	450	475	500	525
Diameter (nm)	425	450	475	500	525
7	0.09	0.34	1.1	3.6	10.3
50	0.1	0.36	1.2	3.8	10.9

It is clear that at temperatures below 450°C evaporation will not play an important role according to this calculation and that the change in mobility equivalent diameter will be almost exclusively due to restructuring and sintering. Therefore, a sintering model can be applied in order to obtain information about the characteristic sintering time. According to Koch and Friedlander (1990) the following expression can be used to account for the reduction of surface area of an aerosol particle being an agglomerate of primary particles:

$$\frac{da}{dt} = -\frac{1}{\tau}(a - a_{sph}) \quad (7.1.3)$$

where a is the surface area of the agglomerate and a_{sph} is the surface area of the equivalent sphere. The characteristic sinter time τ can be written in the following form, in which the dependencies on the temperature and the primary particle size are separated:

$$\tau = c_1 T d_p^n e^{c_2/T} = \tau' d_p^n \quad (7.1.4)$$

where c_1 and c_2 are constants, T is the temperature, τ' is some temperature-dependent sintering function, which is however independent of the primary particle diameter, n is a coefficient which varies with the sinter mechanism which is still unknown for PbS nanoparticles ($n=3$ for volume sintering, $n=4$ for grain boundary or surface sintering) and d_p is the diameter of the primary particles composing the agglomerate:

$$d_p = \frac{6v_{sph}}{a} \quad (7.1.5)$$

in which v_{sph} is the volume of the equivalent sphere. The reason for separating the dependencies of the characteristic sinter time on the primary particle diameter and the temperature is that both parameters are varying in the experiments. For substances with well-known properties, the constants c_1 and c_2 can be calculated (see e.g. Kruis *et al.* (1993) for Si), but for PbS these parameters are not available. Therefore, they are determined on the basis of the experimental data.

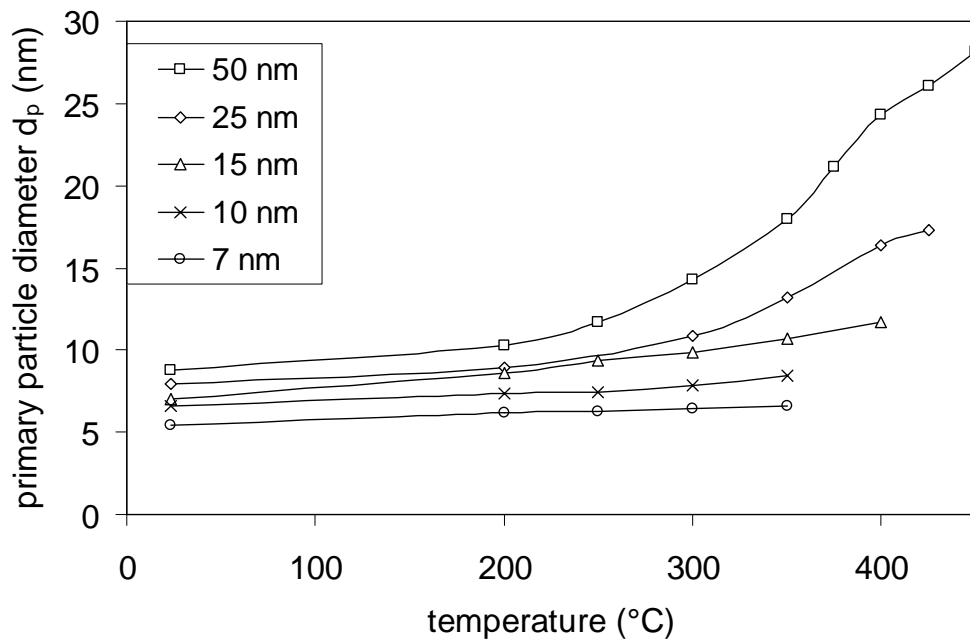
According to Seto *et al.* (1995), the diameter of primary particles can be determined from experiments using:

$$d_p = \frac{d_{sph}^3}{d_m^2} \quad (7.1.6)$$

This bases on eq. (7.1.5) with the assumption that the mobility diameter for nonspherical particles is related to its surface area. Using the measurements of d_m from Fig. 7.1.4, we still need to know the diameter of the particle when sintering is completed, i.e. d_{sph} , for which the mobility diameter at the temperature before evaporation starts is taken. It is estimated that the sintering is complete at 450°C for particles having an initial mobility equivalent diameter of 50 nm, at 425°C for 25 nm, at 400°C for 15 nm, at 375°C for 10 nm and at 350°C for 7 nm. This is based on the experimental observations of the sudden increase of the half-width of the size distribution above these temperatures (Fig. 7.1.5), which are consistent with TEM observations of particle morphology at different sintering temperatures and initial mobility diameter. This enables us to calculate the primary particle size d_p (Fig. 7.1.8a) and consequently the number of primary particles in an aggregate (Fig. 7.1.8b).

The initial primary particle diameter of 5 to 10 nm is in agreement with TEM observations. The larger number of primary particles in an agglomerate for particles with larger initial mobility diameters in the case without sintering (at a temperature of 20°C) has also been observed by means of TEM investigations. It has often been observed in gas-phase processes that agglomerates of different sizes differ mainly in the number of primary particles, not so much in primary particle diameter. This is due to strong dependence of the characteristic sinter time τ on the primary particle size d_p according to eq. (7.1.4), so that during the initial agglomerate formation just after the first furnace the sintering stops when the primary particle size reaches a certain size. It is also possible to simulate numerically the sintering by solving the equations (7.1.3) – (7.1.5) for the given residence time in the second furnace, using the initial conditions obtained from the experiments and using a given value of the sintering function τ' which is constant at a given temperature. It is possible to obtain information about the values of τ' by means of a comparison of the primary particle diameter obtained from the experiments (Fig.7.1.8a) and from the simulations as a function of temperature. The results are shown in Fig. 7.1.9 for two different values of the coefficient n .

a)



b)

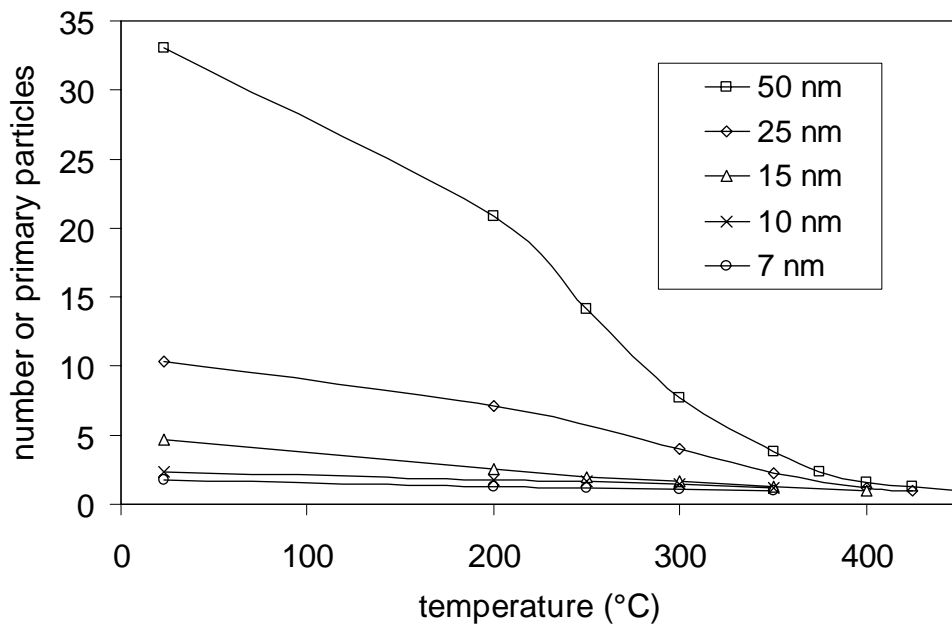


Fig. 7.1.8. (a) Primary particle diameter d_p , calculated from experiments on the basis of eq. (7.1.6) as function of the sintering temperature and initial mobility equivalent diameter of the corresponding agglomerate and (b) the corresponding number of primary particles in an agglomerate.

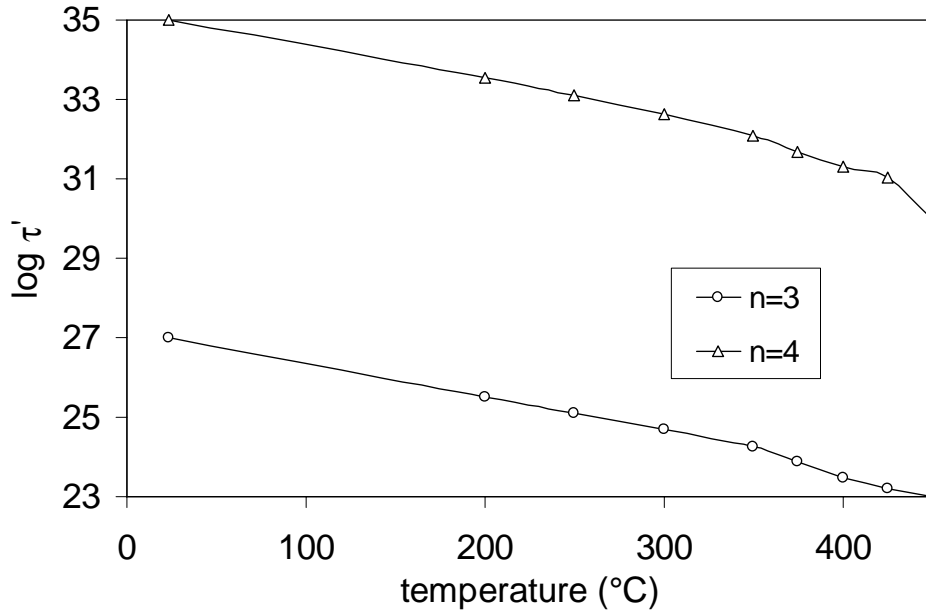


Fig. 7.1.9. Temperature-dependent sintering function τ' determined by comparison of the primary particle diameter extracted from experiments (eq. 7.1.5) and from numerical simulations (eq. 7.1.3). Curves fitted according to eq. (7.1.4) are also shown.

Also shown in Fig. 7.1.9 are the functions fitted to the data according to eq. (7.1.4): $\tau' = 6.068 \cdot 10^{17} T \exp(4898/T)$ for $n=3$ and $\tau' = 5.787 \cdot 10^{22} T \exp(9065/T)$ for $n=4$, with T expressed in K. A slight change in the slope of the data based on the experiments occurs for both coefficients above 350°C, which might be indicative for two different sintering regimes. This change is, however, too small to enable a clear division between two regimes. It is not possible either to assign clearly a sinter mechanism to this system, as there is not a clearly better fit for one of the coefficients. Both combinations of coefficient and temperature-dependent sintering function τ' might be used in predicting the sintering of PbS.

7.2 Preparation of size-classified SnO_x nanoparticles in the gas phase for gas-sensing applications

Tin oxide is one of the most important semiconducting materials for gas sensors. Its electrical properties change as a result of the adsorption of gases onto the surface, as described in Chapter 5.3. In view of the high specific surface and activity of tin oxide nanoparticles, considerable improvement in sensing properties

is expected. In order to understand the relationship between gas-sensing behaviour and particle size better it is necessary to generate monodisperse nanoparticles, because a distribution of particle sizes will decrease the special properties and complicates the interpretation of the experimental results. This was also emphasized by Göpel and Schierbaum (1995) in their review article on future prospects of SnO₂ gas sensors: 'Particular emphasis is put on preparing thin films of SnO₂ with homogeneous particle sizes in the nanometre range'. At the moment no gas sensors based on almost single sized particles are available. A similar technique as described in the preceding section is applied here to synthesize monodisperse SnO_x nanoparticles. The subscript 'x' is used in order to stress that stoichiometry is here not necessarily obtained, in fact some oxygen deficiency is desirable.

7.2.1 Experimental set-up

The experimental set-up is similar to the PbS synthesis set-up, the difference is however that in the second tube furnace a combined oxidation-sintering step is performed. Sn (99.999 %, Aldrich, Germany) is evaporated to form a Sn aerosol in the tube furnace 1. In a second experiment SnO powder (>99 %, Aldrich, Germany) is used. Nitrogen obtained from evaporating liquid nitrogen is used as carrier gas. The system is operated at atmospheric pressure. The gas flow through the furnace was kept at 1.5 l/min.

In the second tube furnace the size-fractionated Sn and SnO nanoparticles can be sintered at different temperatures in order to obtain quasi-spherical particles, as the as-formed particles are agglomerates. The oxidation rate of the nanoparticles can be adjusted in the second tube furnace by means of an oxygen flow, controlled by a MFC. A second DMA allows on-line monitoring of the change in the particle size distribution due to the sintering and/or oxidation in the second furnace.

7.2.2 Results of structural and electrical characterization

The DMA monitoring technique allows fast optimization of the process conditions. For each desired particle size, the evaporation temperature in the first tube furnace has to be tuned for getting the maximal particle number concentration, whereas the final particle morphology and composition depends on the temperature of the second furnace. It was found for Sn as evaporation material that the maximum particle amount shifts to larger particle sizes and that the total quantity of the particles increases with increasing evaporation temperature. When the temperature of the second tube furnace was increased up to 750°C, the curves

shifted to smaller particle sizes and the maximum particle number concentration decreased with increasing temperature. Two mechanisms can be responsible for this phenomenon: the first is a compaction process caused by restructuring, sintering and crystallisation. The second mechanism is evaporating of the particles. In this system, increasing the temperature from 600 °C to 750 °C did not change the mean particle diameter any more, which decreased from 10 nm to 6 nm due to restructuring and sintering.

The evaporation of Sn was not a stable process, however. This can be attributed to contamination of the carrier gas with oxygen. Therefore the evaporating material was changed to SnO, resulting in stable particle concentrations over several days. In Fig. 7.2.1 the particle size distributions are shown when changing the evaporation temperature. The sintering of the size-fractionated aerosol (Fig. 7.2.2) shows the compaction and sintering behavior already encountered for PbS. However, with temperatures above 670 °C a bimodal particle size distribution appears if SnO is evaporated due to a evaporation-recondensation mechanism (Fig. 7.2.3). Here, the SnO vapour from the evaporating particles condenses after leaving the sintering furnace, leading to a new particle fraction with smaller diameter together with the fraction of partly evaporated particles.

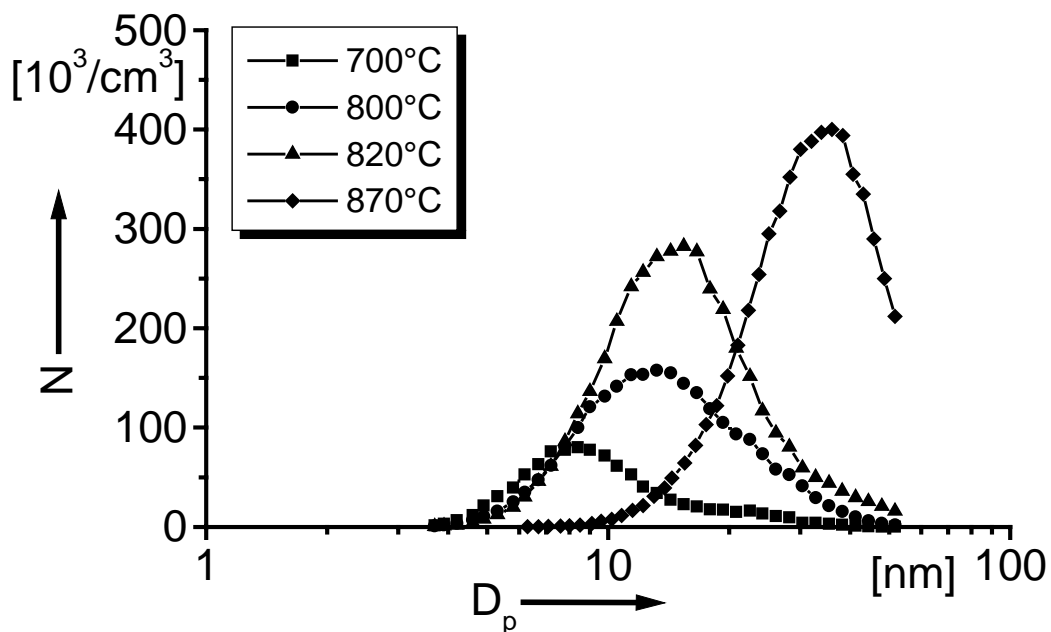


Fig. 7.2.1. Particle size distribution when using SnO as evaporation material at different evaporation temperatures in the first furnace.

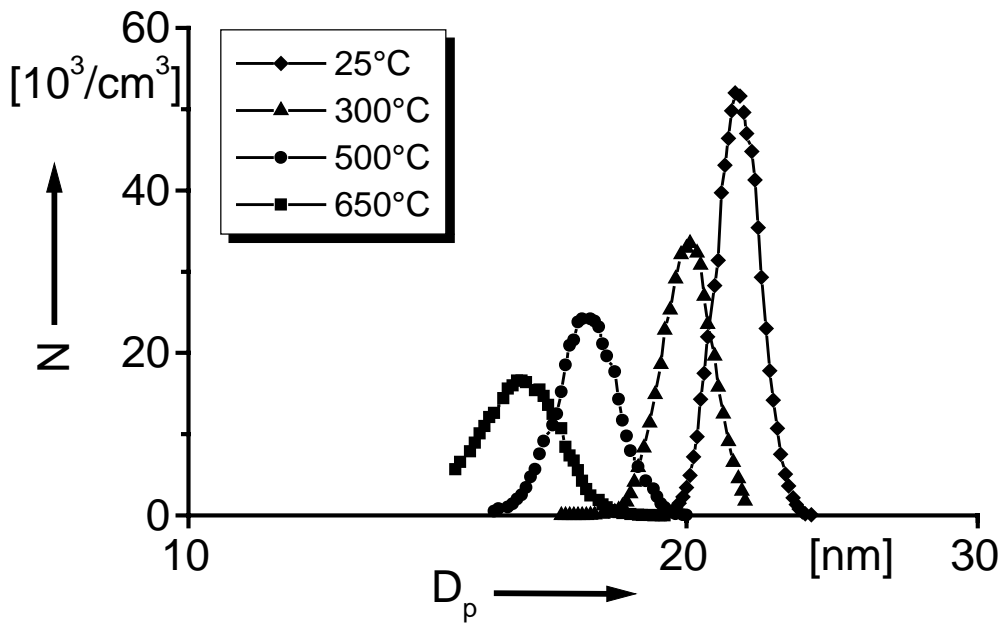


Fig. 7.2.2. Particle size distribution of a size fractionated SnO aerosol ($D_p=15$ nm) at different sintering temperatures in the second furnace (evaporation temperature 800 °C).

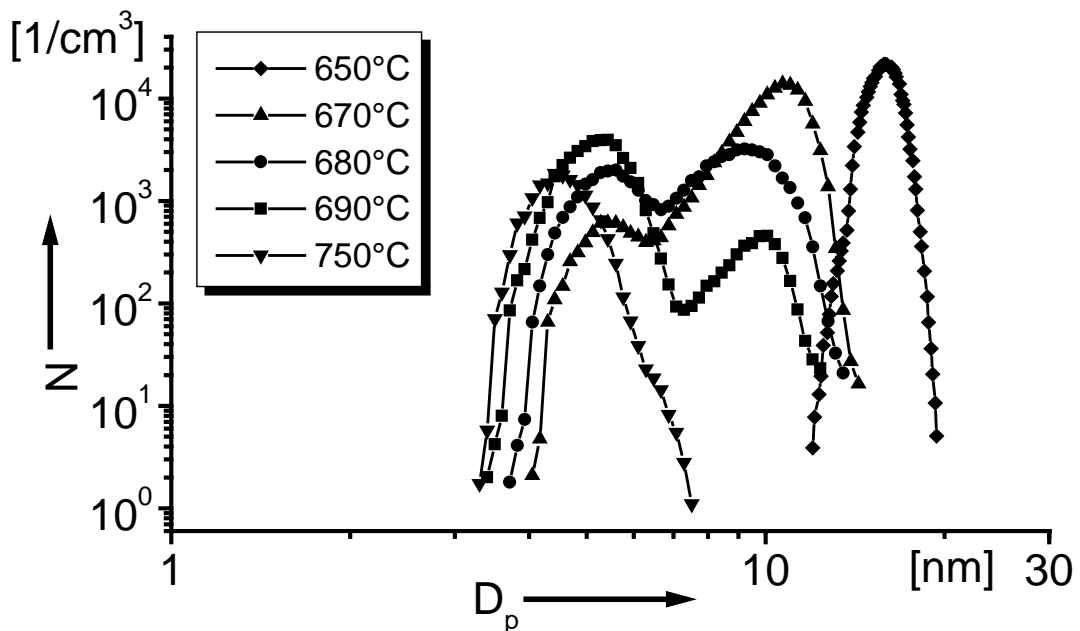


Fig. 7.2.3. Similar to Fig. 7.2.2, with the insert as sintering temperature, now showing a bimodal distribution at a sintering temperature above 670 °C.

It is remarkable that after a running time of several days, the evaporation behaviour of Sn and SnO becomes similar. This can be understood on the basis of the vapour pressures of these materials. The vapour pressure of SnO is much higher compared to Sn at the same temperature, leading to more condensable material in the gas phase. This explains the higher particle concentrations measured in the SnO system. If the carrier gas contains a small amount of O₂, it is assumed that Sn will be oxidized and will evaporate due to the high vapour pressure of the SnO. Another possibility would be to use SnO₂ as starting material, but SnO₂ decomposes into SnO and O₂ upon heating so that this is not a stable evaporating system.

In order to investigate the morphology of the synthesized nanoparticles, TEM micrographs were made. In Fig. 7.2.4 a TEM micrograph is shown of SnO_x nanoparticles coming from the first furnace, i.e., without size-fractionation and sintering/oxidation. The particles are clearly not monocrystalline and monodisperse, they show however appreciable necking due to sintering, which took place during the cooling down after the first furnace. The TEM micrographs of size-fractionated and sintered nanoparticles (Fig. 7.2.5) show much more homogeneous particles. Electron diffraction was used to identify the crystalline structure.

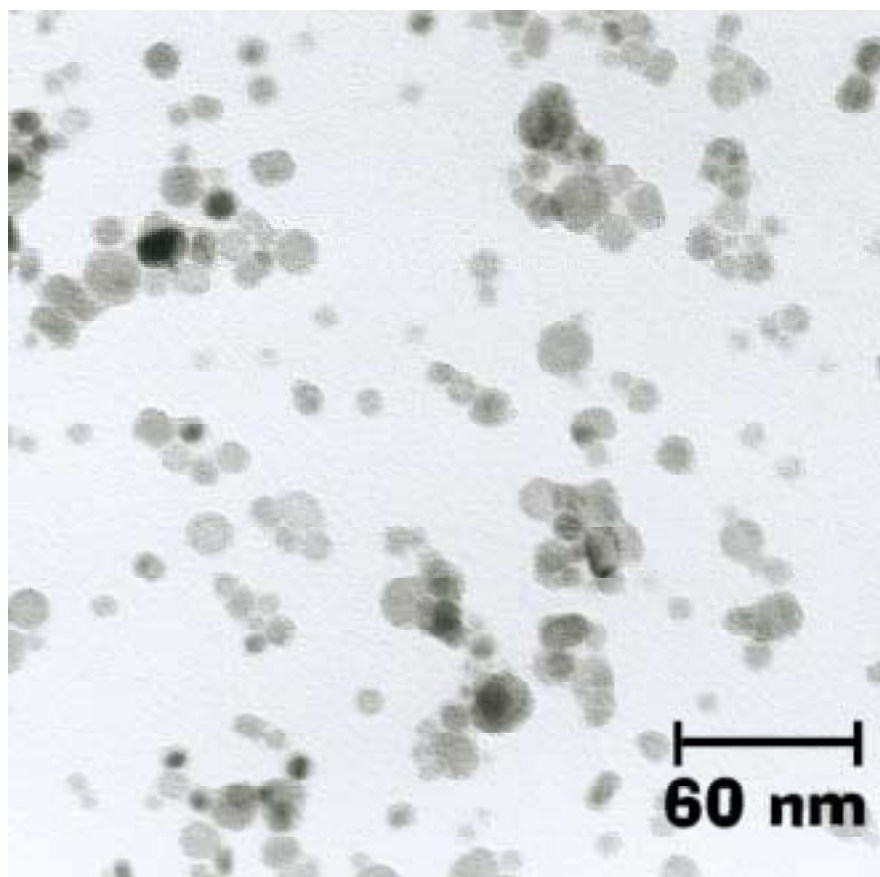


Fig. 7.2.4. TEM micrograph of unfractionated SnO_x nanoparticles coming from the first tube furnace (T=870°C).

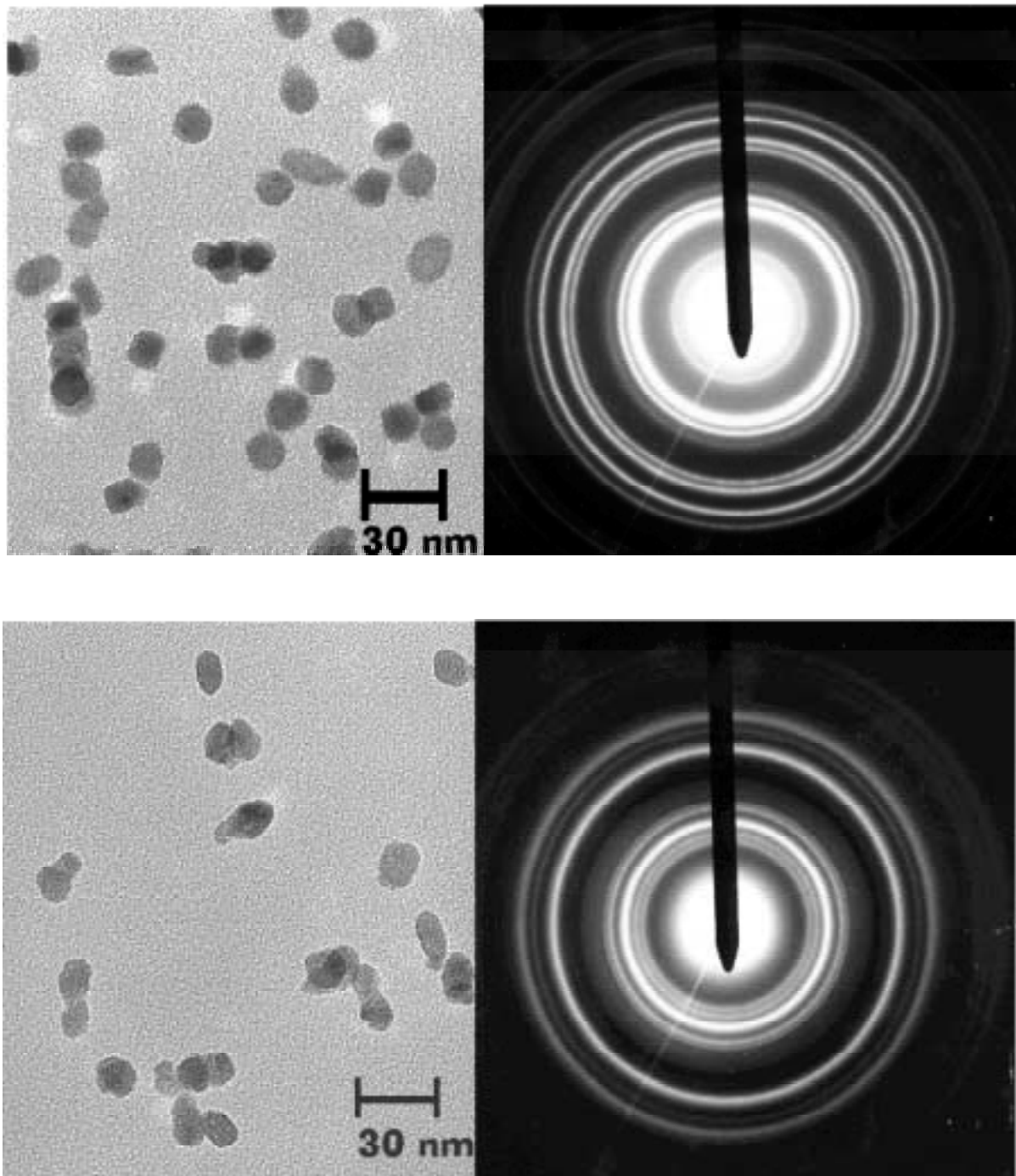


Fig. 7.2.5. TEM micrographs of fractionated SnO_x nanoparticles a) without addition of O₂ in the sinter furnace and b) with addition of O₂ (evaporation temperature 820°C, sintering temperature 650°C, D_p=20 nm). The electron diffraction patterns are characteristic of romarchite (a) and cassiterite (b).

The crystal structure of the nanoparticles which were sintered without addition of oxygen shows a tetragonal crystal structure, romarchite, characteristic for SnO. When a flow of O₂ was added to the SnO aerosol flow in the sintering furnace, so that the O₂ percentage was approximately 50 vol%, the crystal structure found was a tetragonal phase, cassiterite, characteristic for SnO₂. Although the exact stoichiometry could not directly be determined, the presence of different crystal structures induced by O₂ addition indicates that it will be possible to vary the stoichiometry by changing the concentration of O₂ in the second furnace.

In order to get a first impression of the feasibility of the synthesized SnO₂ nanoparticles for use in gas-sensing investigations, an electrical characterization was carried out. To this end, an approximately 0.2 μm thick film of nanoparticles with a diameter of 35 nm after size-fractionation was deposited on a glass substrate. The film was electrically contacted by means of silver paste and the *I-V* characteristic was measured (Fig. 7.2.6). The addition of 0.5 vol% CO, which is a reducing gas, increases the current at constant voltage. Thus, the resistance decreases, which is expected according to the qualitative model described in Chapter 5.3, which states that a reducing gas decreases the concentration of chemically absorbed oxygen so that the conductivity increases.

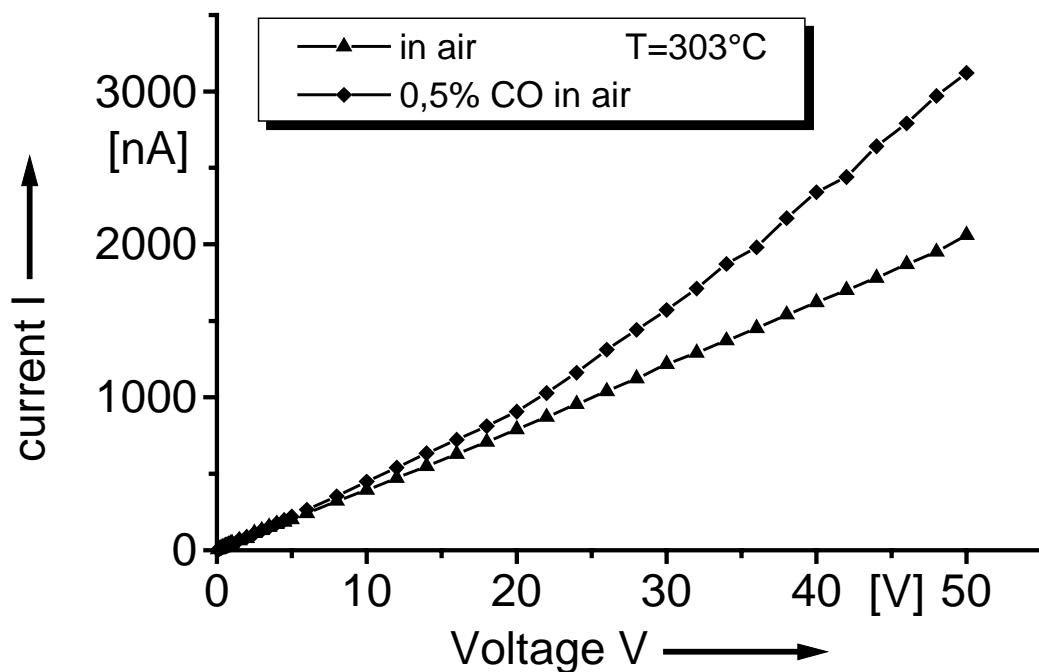


Fig. 7.2.6. *I-V* characteristics of a thin film (~0.2 μm) of SnO₂ nanoparticles which were 35 nm in diameter after sintering at 650°C. The film itself has not been sintered.

Gas sensors detect changes in the gas concentrations by measuring changes of the resistance of the sensor in a certain gas atmosphere, R_g , when compared with its resistance in pure air, R_a . Therefore, the sensitivity, defined here as R_a/R_g , is shown in Fig. 7.2.7 and shows the expected increase with temperature, most probably due to the changes in surface chemistry with temperature. This increased sensitivity is the reason why gas sensors are operated at higher temperatures, usually between 200 and 400°C.

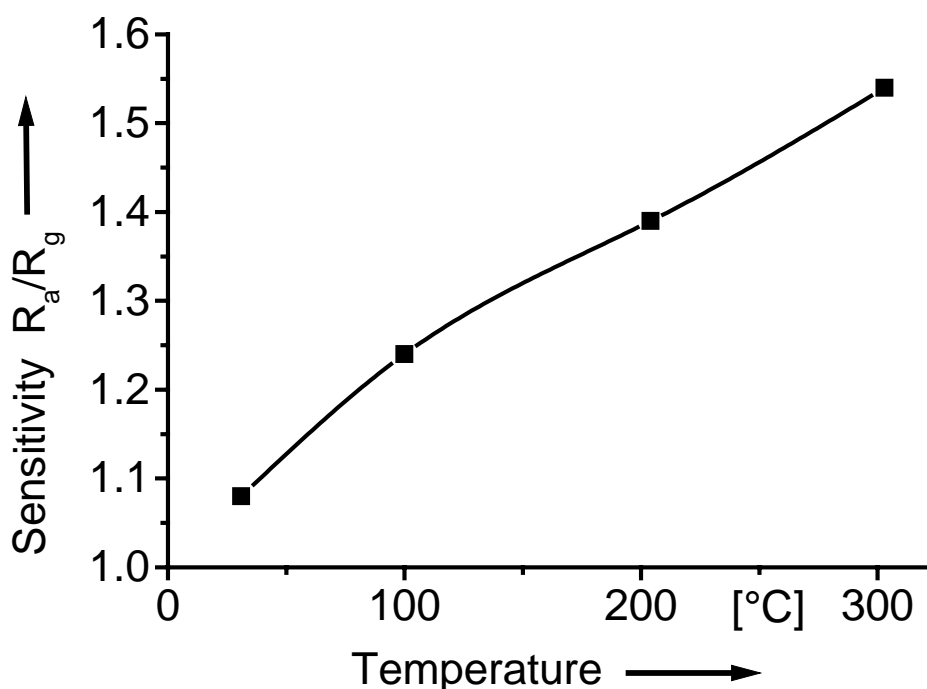


Fig. 7.2.7. The sensitivity R_a/R_g of a thin SnO₂ film (described in Fig. 7.2.5) in 0.5 vol% CO as a function of the temperature in the measurement cell.

Another important characteristic of a gas sensor is its response time. This is tested by changing rapidly the gas atmosphere, in Fig. 7.2.8 from a CO atmosphere to air and back to CO. Due to the use of a flow system and a small volume of the measurement cell, it takes some 5 s to exchange the gas atmosphere. It can be seen from the figure that the change on adding CO is relatively rapid, in the order of 2 minutes, while it takes longer to recover when the CO is not any more present. It is clear that the process is not completely reversible, presumable due to the complicated relationship between chemistry and material properties.

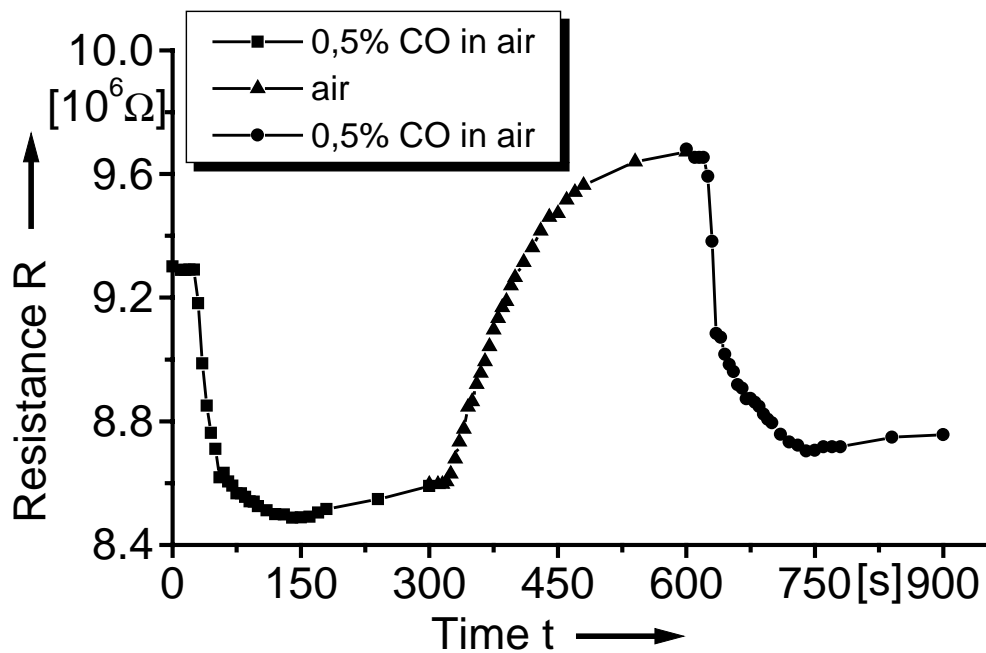


Fig. 7.2.8. The time-dependence of the resistance of the thin SnO_2 layer (described in Fig. 7.2.6) when changing the gas atmosphere from 0.5 vol% CO to air and back to 0.5 vol% CO ($T=303^\circ\text{C}$)

The measurements shown were done for thin films which were not yet sintered, so that the interparticle contacts, which are essential for the gas-sensing mechanism, were probably not yet fully established. These preliminary measurements show that it is possible to create thin gas-sensitive layers composed of equal-sized SnO_2 nanoparticles. The experimental procedure allows to produce thin films, in which the properties of the nanoparticles can be independently controlled by size-fractionation and in-flight sintering and oxidation. In the usual thin film synthesis techniques, such as sputtering and vacuum-evaporation, the particle formation and film formation take place in one step, so that the control over the final morphology of the nanostructured film is not as good as in the method described here.

7.3 Quantum confinement in size-classified PbS nanoparticles

As already discussed in Chapter 2.1, it is well known that semiconductor nanocrystals exhibit quantum confinement effects when the particle size is of the order of the Bohr exciton. This is indicated by a blue shift in the optical absorption spectra. PbS is an attractive candidate for the study of quantum confinement effects as the Bohr radius is 9 nm and the effect in PbS nanoparticles synthesized by different chemical routes are well studied (Wang *et al.*, 1987, Zhao and McCormick, 1992, Salata *et al.*, 1994a). Quantum confinement effects have also been observed in evaporated composite films of PbS nanoparticles (Thielsch *et al.*, 1998). In this subchapter, quantum confinement effects in PbS nanoparticles synthesized in the gas phase are reported. Advantages of the gas-phase synthesis method described earlier in this chapter over liquid-phase synthesis methods for investigating quantum confinement effects are the possibility of size-fractionation and the absence of ligands and other impurities. Furthermore, the sintering process involved in the synthesis allows control over crystallinity and shape.

7.3.1 Experimental methods

Single crystalline PbS nanoparticles with different crystalline sizes are synthesized by the gas phase technique described earlier in this chapter. For the optical absorption studies, different crystalline sizes are sintered at different temperatures. The names of the samples are given according to the initial mobility diameter. In this context it is worth pointing out that the size and shape of the particles depend on the sintering temperature. The sintering temperatures are well below the respective evaporation temperatures. Several monolayers of nanoparticles were deposited by means of the electrostatic precipitator onto a glass substrate.

The optical absorption spectra at room temperature were recorded using a Beckman-spectrophotometer (Model UV-5240) which is able of recording spectra between 300 and 3000 nm. For this, a bare glass plate was put in front of the reference beam while the glass substrate with PbS films was placed in front of the sample beam. The thickness of the PbS layers was estimated by knowing the area of deposition, the rate of deposition and the size of the particles deposited with the assumption that the particles are spherical. The absorption spectra were normalized with respect to the thickness of the film thus estimated.

7.3.2 Results and discussion

The optical absorption spectra for PbS nanoparticles with different sizes are shown in Fig. 7.3.1. As PbS is a direct band gap semiconductor, the band gap can be determined from the plot $(\alpha h\nu)^2$ vs $h\nu$ by extrapolating $(\alpha h\nu)^2$ to zero value, where α is the absorption coefficient and $h\nu$ is the photon energy. The band gap is the value of $h\nu$ for which $(\alpha h\nu)^2$ is zero. The large blue shift in the absorption spectra with respect to the bulk band gap of 0.4 eV is indicative of the quantum confinement effect.

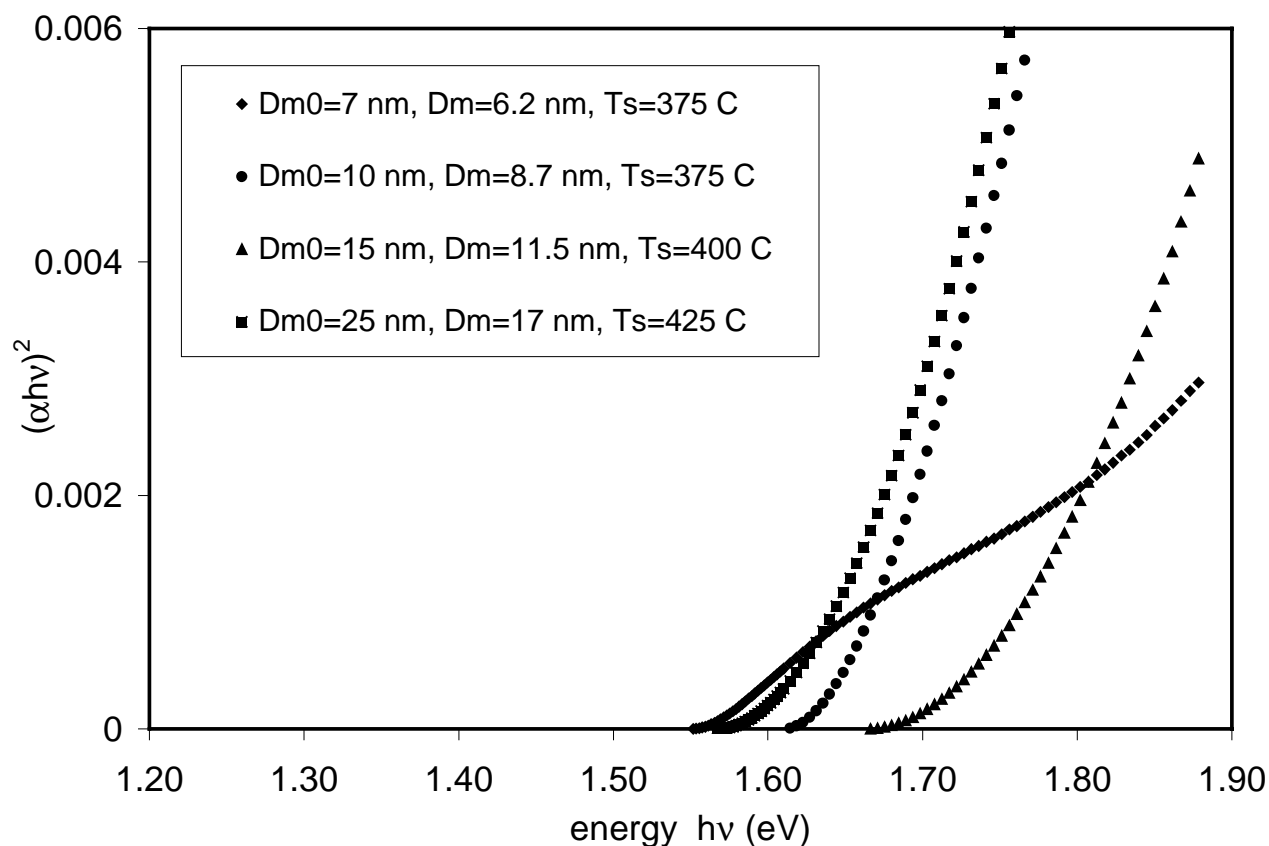


Fig. 7.3.1. The optical absorption spectrum (normalized with respect to film thickness) of PbS nanoparticles of different sizes (D_{m0} is the initial mobility diameter and D_m is the mobility diameter after in-flight sintering at T_s)

It can be seen from the figure that the band gaps of the particles with mobility diameters between 6 and 17 nm are all between 1.5 and 1.8 eV, whereas this band gap range was found for PbS nanoparticles synthesized in a liquid between 3 and 4 nm, as can be seen from Fig. 2.1. Several explanations are possible. The mobility diameter is not related in any way to the crystallite size. A particle might be polycrystalline and be composed of several smaller crystallites, so

that a larger bandgap would result. Another possibility is that the particles are composed of a crystalline core with an amorphous shell or even an oxide layer, which would reduce the effective crystallite diameter. Furthermore, the literature data (as shown in Fig 2.1) are for particles suspended in a liquid and protected against aggregation by means of organic ligands, which might influence their electronic properties. The compact PbS nanoparticle films investigated here do not have such ligands, but the nanoparticles have no or very small interparticle distances, which also might influence their properties. Finally, the possibility exists that the particles are non-spherical. When they are in the form of platelets, this is difficult to detect using TEM, and the smallest particle dimension tends to have the largest influence on the quantum confinement (Zhao and McCormick, 1992).

The comparison between the samples with different diameters is difficult due to the fact that both the initial mobility diameter and the sintering temperature play a role. An attempt to elucidate the effect of sintering temperature is shown in Fig. 7.3.2.

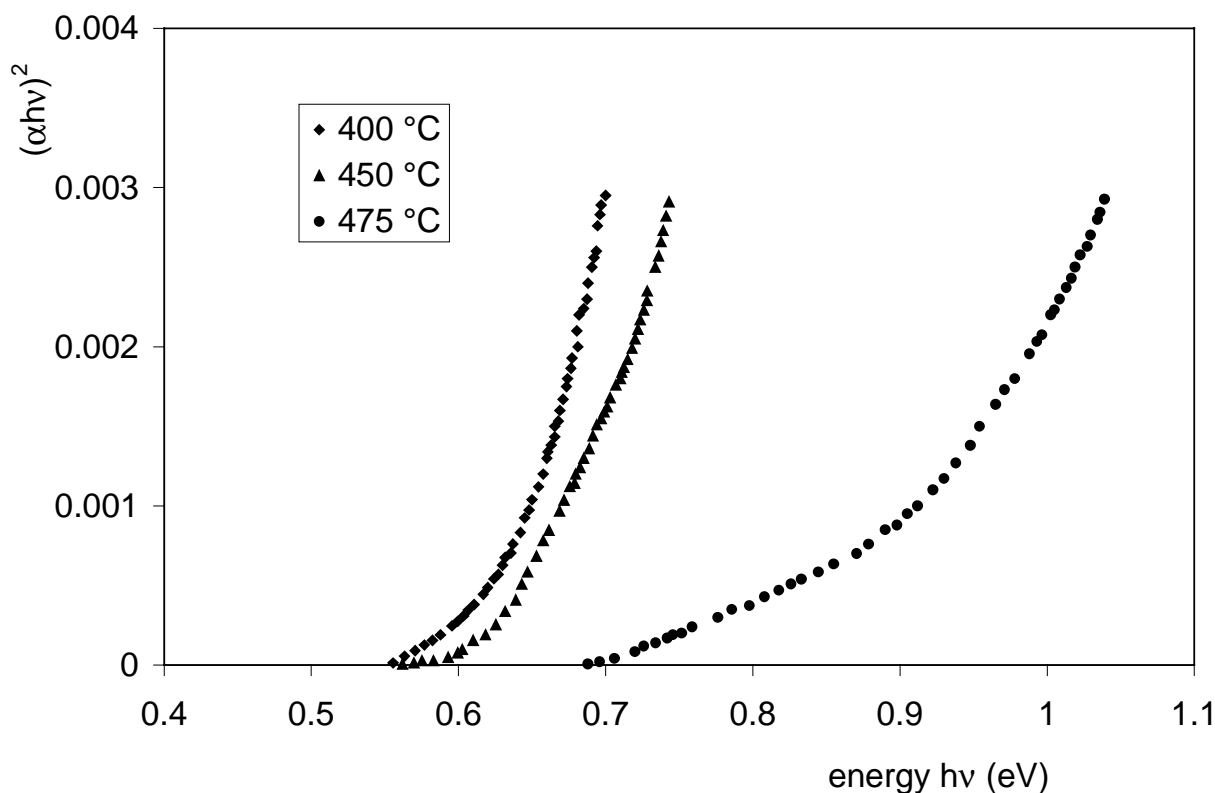


Fig. 7.3.2. The optical absorption spectrum (normalized with respect to film thickness) of PbS nanoparticles with an initial mobility diameter of 50 nm and sintered at the temperature indicated.

As discussed in subchapter 7.1., the geometry of the particles depends on the sintering temperature. When the sintering temperature is increased, the mobility equivalent diameter is found to decrease - a consequence of the restructuring, sintering and crystallisation. Furthermore, evaporation can play a role above a certain temperature which is particle size-dependent. For the particles sintered at 400°C and 450°C, there is little difference observed in the absorption and the band gap does not change clearly. At 475°C however, the bandgap is shifted toward the blue which is an indication for smaller particles. This agrees very well with the results from subchapter 7.1. – evaporation which reduces particle size is negligible at 450°C and starts taking place at 475°C.

Another effect which was found to influence the experimental results, is the time between film deposition and measurement of the optical absorption spectrum. As can be seen in Fig. 7.3.3, the band gap shifts to a higher value one month after deposition, but then seems to be stable. The change in the band gap might be due to oxidation of the nanoparticles, as they were stored in air, or due to morphological changes, as in TEM observations sintering at room temperature has been observed.

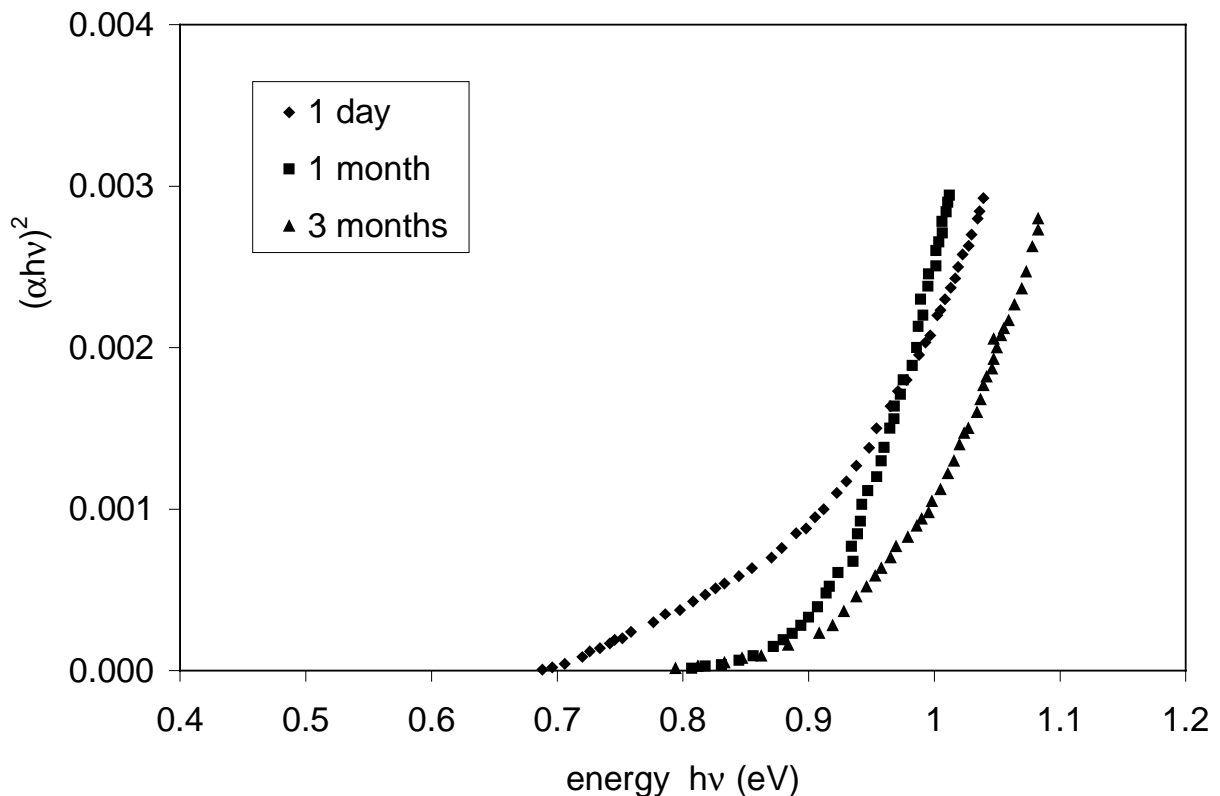


Fig. 7.3.3. The optical absorption spectrum (normalized with respect to film thickness) of PbS nanoparticles with an initial mobility diameter of 50 nm and sintered at 475 °C at different times after deposition.

When comparing the band gaps for the samples having initially a mobility diameter of 50 nm, in the range 0.6-0.7 eV, and for the samples having a mobility diameter of 25 nm or smaller, in the range 1.5-1.8 eV, it is interesting to see that the range of 0.7-1.5 eV is not yet covered. This range contains the commercially interesting range around 1.3 eV, used for very fast optical data transfer by means of GaAs solid state lasers. By choosing initial mobility diameters in between 25 and 50 nm, it should be possible to attain this band gap. Further investigations should be accompanied by careful observations of the actual particle diameter and crystallinity after sintering at different temperatures, preferably by means of high-resolution transmission microscopy.

7.4 Experimental investigation of synthesis of tailored composite nanoparticles in the gas phase

A special case of nanostructured materials is formed by composite particles, here defined as aggregates composed of two different particle classes. Three different basic classes of such composite particles can be distinguished (Fig. 7.4.1):

- a single particle containing two compounds mixed on an atomic scale,
- a 'core-shell' particle, in which the core and the shell are composed of different compounds,
- a 'nanoaggregate', which is a compound particle consisting of two particles of different chemical composition

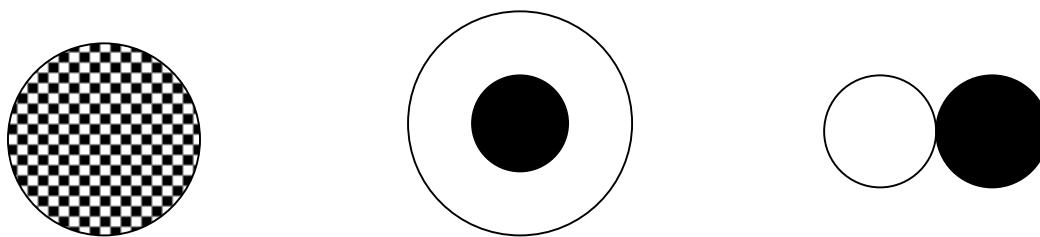


Fig. 7.4.1. Basic classes of composite nanoparticles: a composite nanoparticle, a core-shell nanoparticle and a nanoaggregate.

The technological use of such particles is manifold, e.g.:

- improve the mixing characteristics when two ultrafine powders have to be mixed: when the powders are mixed in aerosol form, the occurrence of large aggregates of one component, which is detrimental for the mixing, can be suppressed,

- improve the functional properties of semiconductor nanoparticles by adding a second semiconductor particle which provides a charge transfer, thereby improving the quantum yield,
- improve the functional properties of nanoparticles by adding another nanoparticle which has catalytic properties, such as Pt or Pd which enhances the sensitivity of SnO₂ nanoparticles used for gas sensors,
- improve the superconductive properties of YBCO particles by adding smaller particle which act as flux pinning enhancement (Takao *et al.*, 1997)

Most methods rely on Brownian aggregation between two different aerosols, which is however difficult to control. Here an experimental procedure is proposed for the controlled synthesis of composite nanoparticles in the gas phase. The theoretical background is already given in Chapter 4.3. Two oppositely charged aerosol flows with different nanoparticles are mixed and the ensuing aggregation will lead to formation of a fraction of composite nanoparticles.

7.4.1 Experimental methods

Nanoparticles of two different substances, PbS and Ag, were generated separately in the gas phase by means of the DMA fractionation technique. and mixed bipolarly. The experimental set up is presented in Fig. 7.4.2.

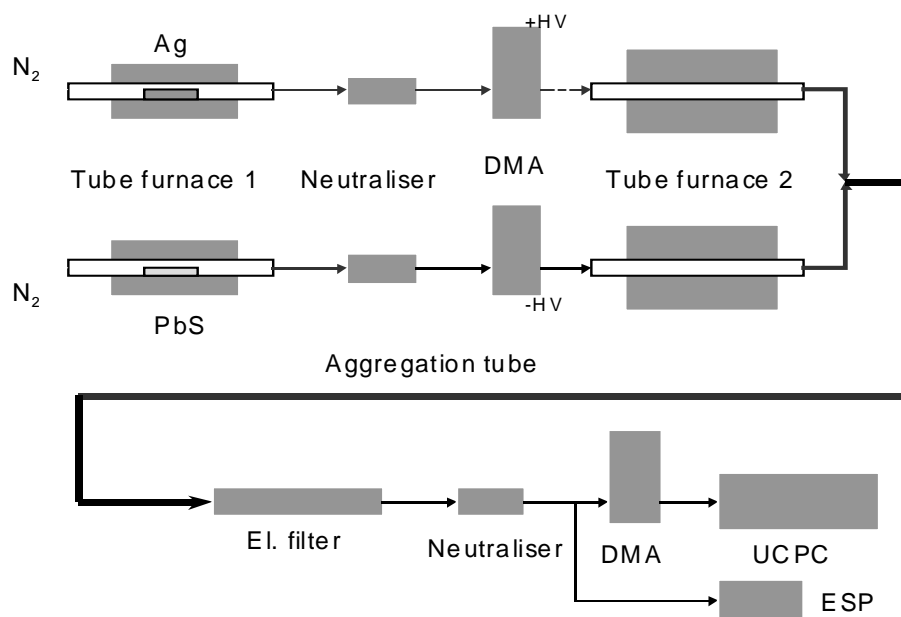


Fig. 7.4.2. Experimental set up for synthesis of composite particle pairs, here PbS and Ag.

The experimental setup contains five main elements: two synthesis units which deliver monosized quasi-spherical nanoparticles of PbS and Ag, an aggregation tube, an electrostatic precipitator and a particle size measurement system. The entire process took place in purified N₂ at 1 bar. The synthesis unit for PbS has been described earlier. Briefly, powders of PbS or Ag are heated at 680°C and 1150°C, respectively, in a tube furnace under flowing N₂ and form particles by homogeneous nucleation in the cooling vapor and subsequent aggregation by Brownian motion. It results in relative broad size distribution. The aerosols are charged bipolarly by a radioactive β-source (Kr⁸⁵) and size-selected by means of a Differential Mobility Analyzer (NANO-DMA, TSI, Minneapolis, USA and VIE06-3/150, HAUKE GmbH, Austria). The DMA selects particles on the basis on their electrical mobility and is operated such that geometric standard deviations of about 1.1 are obtained. Applying voltages of opposite polarities inside the DMA's one can obtain oppositely singly charged aerosols. The irregularly-formed aerosol particles are then sintered in-flight ($t_{\text{sinter, Ag}} = 400^{\circ}\text{C}$, $t_{\text{sinter, PbS}} = 475^{\circ}\text{C}$) in order to obtain quasi-spherical nanoparticles, which facilitates their identification. The values of particle number concentrations for both components were approximately matched (between $7.0 \times 10^4 \text{ cm}^{-3}$ and $9.5 \times 10^4 \text{ cm}^{-3}$), measured by means of a condensation nucleus counter (UCPC, TSI, Minneapolis, USA).

Both the PbS and Ag aerosols with quasi-spherical, monosized and oppositely charged nanoparticles were lead to the aggregation tube, which consisted of copper tubes with a length of 5 or 10 m and a diameter of 20 or 32 mm. The resulting size distribution was measured by a measurement setup consisting of a bipolar charger, a DMA and a condensation nucleus counter. To remove the remaining charged particles, the aerosol flow could be passed through an electrostatic filter so that only electrically neutral particles came through. An electrostatic precipitator (ESP) was used to deposit these selected composite nanoparticles on a TEM grid after recharging them by means of an excimer lamp ($\lambda = 172 \text{ nm}$) or a radioactive source.

7.4.2 Results and discussion

The resulting particle size scans after mixing oppositely charged Ag and PbS nanoparticles with diameters of about 20 and 24 nm, respectively, are shown in Fig. 7.4.3 for different residence times in the aggregation tube. Again, these scans have not been corrected for charging efficiency of the radioactive source and transmission efficiency of the DMA, and are strictly speaking no size distributions. The curves show three features: the first two corresponding to primary,

unaggregated nanoparticles and the third corresponding to nanoaggregates. When applying electrostatic filtering, only the uncharged nanoaggregates with an effective mobility diameter of 30 nm are left. It can be seen that doubling the residence time in the aggregation tube increases the number of nanoaggregates approximately by a factor of two, which is in accordance with aggregation kinetics.

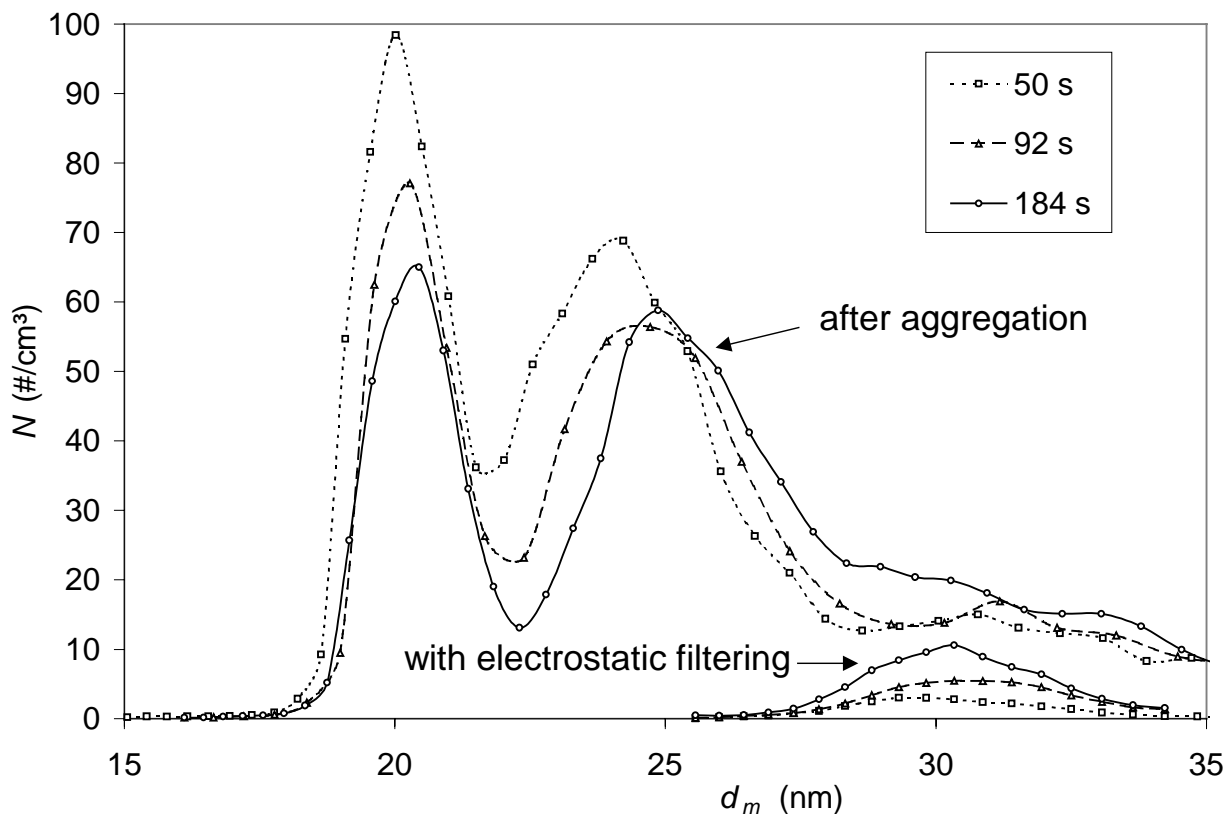


Fig. 7.4.3. Scan over the particle mobility diameter of the resulting aerosol after different residence times in an aggregation tube when Ag and PbS nanoparticle aerosols with diameters of about 20 and 24 nm and a one negatively and positively elementary charge, respectively, are mixed. Also shown are the corresponding scans after applying electrostatic filtering, so that only uncharged particles which are Ag-PbS nanoaggregates are left.

The relative low value of the primary particle concentrations N_{Ag} and N_{PbS} due to the size-selection results in low values of composite particle concentration N_{Ag-PbS} , which can be estimated from $dN_{12}/dt = \beta_{12}N_1N_2$, so that long residence times are necessary. As particle diffusion losses to the walls of the aggregation tube do not depend on the diameter of the tube for a given volumetric flow but increase

with the tube length, increasing the diameter of the aggregation tube seems to be the best way to obtain a larger residence time and thus a higher concentration of composite nanoparticles. With the largest residence time some 7% of the primary particles are aggregated in form of composite nanoparticles, so that after electrostatic filtering a concentration of $7 \cdot 10^3 \text{ cm}^{-3}$ of composite nanoparticles is obtained.

An additional information contained in Fig. 7.4.3 is the direct experimental determination of the mobility diameter for aggregates consisting of two well-defined primary particles. The aggregate mobility diameter can be estimated using the concept of fractal dimension. In this approach, the value of the mobility diameter d_m depends on the primary particle diameter d_0 , number of primary particles in the aggregate n and the fractal dimension D_f as follows:

$$d_m = d_0 n^{D_f} \quad (7.4.1)$$

This equation was shown to be valid for small aggregates ($n < 20$) in the free molecular regime, for which a fractal dimension of 2.18 was experimentally found (Cai and Sorensen, 1994). Using eq. (7.4.1) yields a mobility diameter of 30.6 nm with the primary particle diameter taken here as the volumetric mean value of the two diameters (20 and 24 nm). This value agrees well with the experimentally found mobility diameter, being about 30 nm.

On transmission electron micrographs of the deposited composite nanoparticles (Fig. 7.4.4) one can clearly see nanoaggregates composed of two primary particles to prevail. Also some nanoaggregates composed of four primary particles were observed, which results from the electrostatic filtering allowing to pass only uncharged aggregates. Uncharged aggregates can be composed of equal numbers of PbS and Ag primary particles. In the TEM micrograph, also some particles look like single primary particles. This might be due to a discharging of primary particles in the aggregation tube or due to one particle being shielded from view by another one.

Electron diffraction shows the presence of both silver and lead sulfide in crystalline form. An EDX line-scan over a single nanoaggregate along a line between the particle centers is shown in Fig. 7.4.5. Both Ag and PbS were detected, the maxima of the distributions being some 13 nm apart which is approximately the distance between primary particle centers as determined from TEM (the insert in the figure). The relatively broad distribution of the components is due to the finite width of the electron beam, here about 10 nm.

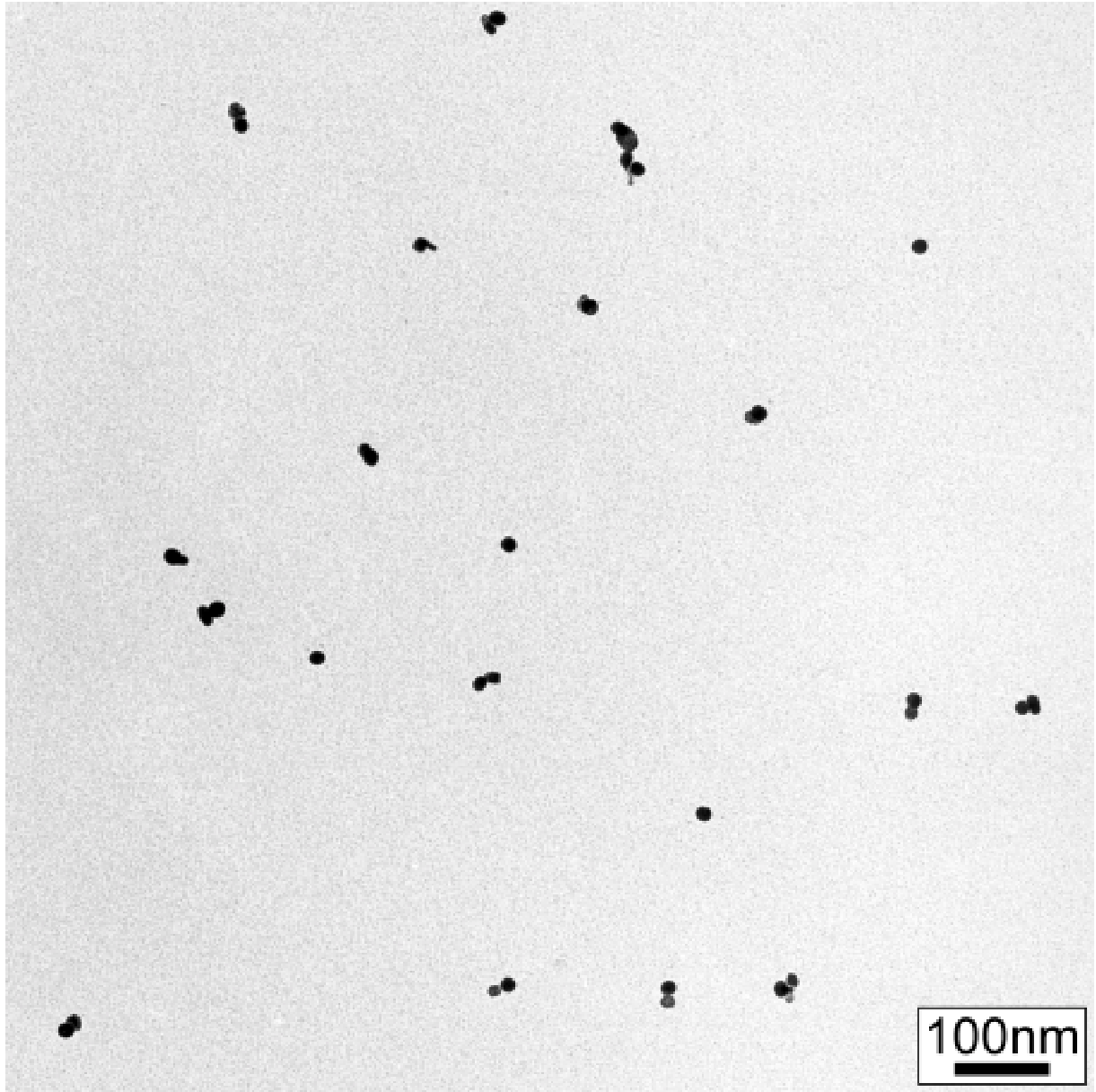


Fig. 7.4.4. Transmission electron micrograph of Ag-PbS nanoaggregates, composed of PbS nanoparticles with a mobility diameter of 17.5 nm and Ag nanoparticles with a mobility diameter of 21.5 nm.

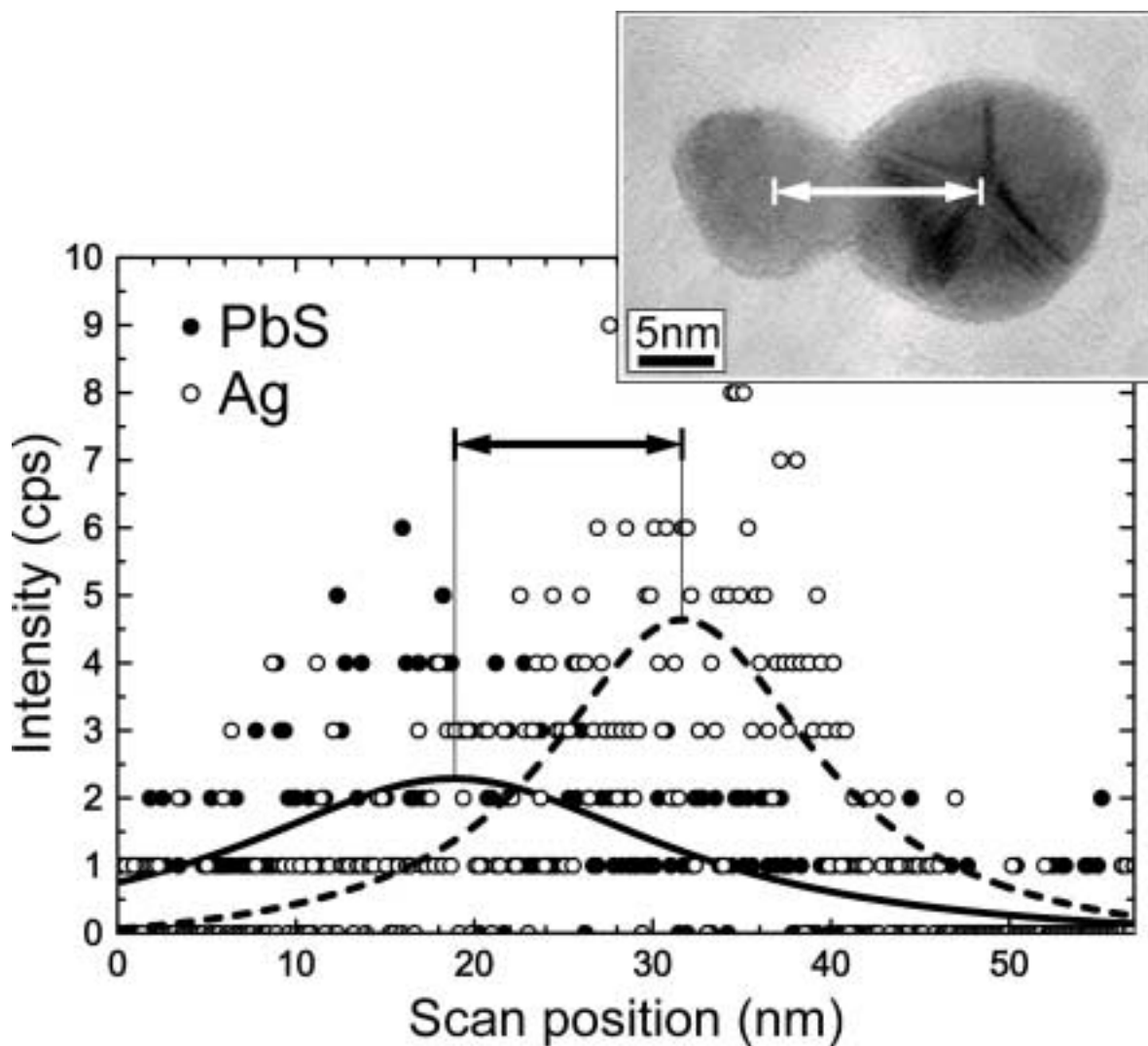


Fig. 7.4.5. EDX line-scan over a nanoaggregate, composed of size-fractionated Ag and PbS primary particles, as described in the caption of Fig. 7.4.4. The insert shows the TEM micrograph of the corresponding nanoaggregate.

Due to the low concentrations of the nanoparticle pairs formed (some 10^3 cm^{-3}), the applications of the method are at present limited to fundamental investigations of the properties of the formed particle pairs, e.g. in optical materials, sensors, solar cells and catalyst and to applications where only very thin layers are needed. Higher concentrations can be reached when the size fractionation step is deleted and two aerosols are mixed after having been charged unipolarly and oppositely, but at expense of the high degree of control in the present process

7.5 Conclusions: Synthesis of PbS and SnO_x nanoparticles for functional applications

Synthesis of the semiconductors PbS and SnO_x is showed to be possible with the help of carefully controlled techniques such as size fractionation and in-flight sintering. With techniques basing on electrical effects, nanoparticle composite pairs have been obtained experimentally. The process of sintering PbS has been investigated for PbS with help of a quantitative model which allowed the determination of sintering parameters. As a first indication of changing physical properties with particle size, the absorption spectrum of PbS particles is shown to shift toward the blue, indicative for quantum confinement effects. Thin films composed of SnO_x nanoparticles show gas-sensitive behavior.